Article

Revisiting the Anomalous Bending Elasticity of Sharply Bent DNA

Peiwen Cong,[1,2,3] Liang Dai,[4] Hu Chen,[5] Johan R. C. van der Maarel,[3] Patrick S. Doyle,[4,6] and Jie Yan[1,3,4,7,*]
[1]Mechanobiology Institute, [2]Singapore-MIT Alliance, and [3]Department of Physics, National University of Singapore, Singapore; [4]BioSystems and Micromechanics IRG, Singapore-MIT Alliance for Research and Technology Centre, Singapore; [5]Department of Physics, Xiamen University, Xiamen, Fujian, China; [6]Department of Chemical Engineering, Massachusetts Institute of Technology, Cambridge, Massachusetts; and [7]Centre for BioImaging Sciences, National University of Singapore, Singapore

ABSTRACT Several recent experiments suggest that sharply bent DNA has a surprisingly high bending flexibility, but the cause of this flexibility is poorly understood. Although excitation of flexible defects can explain these results, whether such excitation can occur with the level of DNA bending in these experiments remains unclear. Intriguingly, the DNA contained preexisting nicks in most of these experiments but whether nicks might play a role in flexibility has never been considered in the interpretation of experimental results. Here, using full-atom molecular dynamics simulations, we show that nicks promote DNA basepair disruption at the nicked sites, which drastically reduces DNA bending energy. In addition, lower temperatures suppress the nick-dependent basepair disruption. In the absence of nicks, basepair disruption can also occur but requires a higher level of DNA bending. Therefore, basepair disruption inside *B*-form DNA can be suppressed if the DNA contains preexisting nicks. Overall, our results suggest that the reported mechanical anomaly of sharply bent DNA is likely dependent on preexisting nicks, therefore the intrinsic mechanisms of sharply bent nick-free DNA remain an open question.

INTRODUCTION

Many cellular processes such as DNA packaging and gene transcription require sharp DNA bending (1,2). Thus, knowledge of the mechanics of sharply bent DNA is critical to understand these cellular processes. DNA is often modeled as a linear polymer that is described by a spatial curve in three dimensions. The bending rigidity of non-sharply bent DNA has been described by the wormlike chain (WLC) polymer model (3). In the WLC polymer model, the bending energy of short DNA is described by $\beta E(\theta;A) = (A/2L)(\widehat{t}' - \widehat{t})^2 = (A/L)(1-\cos\theta)$, where A is the bending persistence length of DNA. Here $\beta = 1/k_BT$ scales energy into units of k_BT; $L << A$ is the DNA contour length; $\widehat{t}, \widehat{t}'$ are the tangent vectors at two DNA ends; and θ is the bending angle of DNA. The bending persistence length of *B*-form DNA has been experimentally determined to be $A \approx 50$ nm (4–7). This bending rigidity is also related to the Young's elasticity modulus Y of elastic rods through the equation $A = \beta YI$. Here $I = \pi R^4/4$ is the DNA area moments of inertia, while R is its radius.

The mechanical anomaly of sharply bent DNA was reported in several recent experiments. In particular, the probabilities of spontaneous looping of ~100 bp DNA into minicircles were several orders of magnitude larger than predicted by the WLC model (8,9). The level of DNA bending in such DNA minicircles is biologically relevant given its similar level of bending to DNA wrapping around nucleosomes (10,11). While the mechanical anomaly of sharply bent DNA has drawn extensive interest, the underlying mechanisms remain unclear and debated. This work aims to provide insights into this debate using full-atom molecular dynamics (MD) simulations. To help readers understand the question and the motivation of this work, we first review previous DNA looping experiments and the underlying assumptions used to interpret those results.

J-factor measurements

The debate surrounding the mechanisms of sharply bent DNA flexibility began with a *j*-factor measurement, which reported an anomalously high probability of DNA looping at 94–116 bp (8). These experiments used a DNA fragment with short strands of complementary single-stranded DNA (ssDNA) overhanging on each end. In a solution at a concentration $c = N/V$ (N is the number of molecules and V is the volume), a terminal end can hybridize with the complementary end on the same DNA fragment (i.e., looping) or with the end of a different DNA fragment (i.e., dimerization), which is driven by thermal fluctuation. Theoretically, the ratio of the looping and dimerization rates predicts the probability density of spontaneous looping in competition with hybridization to a nearby DNA molecule. This probability density is determined by *j*-factor measurements with the following equation: $\rho^J(\mathbf{0}) = c' \times (r_{loop}/r_{dimer}) = (c'/c) \times (r_{loop}/r^0_{dimer})$. In this equation, $\mathbf{0}$ indicates zero end-to-end distance vector, $c' < c$ is the concentration of DNA fragments with orientations

Submitted April 14, 2015, and accepted for publication October 9, 2015.

*Correspondence: phyyj@nus.edu.sg

Editor: Jason Kahn.

0006-3495/15/12/2338/14

http://dx.doi.org/10.1016/j.bpj.2015.10.016

allowing for hybridization, and $r^0_{\text{dimer}} = r_{\text{dimer}}/c$ denotes the dimerization rate per unit concentration of DNA. The superscript J indicates that $\rho^{\text{J}}(\mathbf{0})$ is determined by *j*-factor measurements.

According to this equation, the looping probability can be experimentally determined from the ratio of looping and dimerization rates, which can be measured by chemically fixing the populations of looped and dimerized DNA species with a ligation reaction (4,12). Importantly, equilibration of the double-nicked DNA intermediates (looped fragments and dimers) before ligation is a prerequisite. In other words, *j*-factor measurements probe the looping probability of a subset of double-nicked looped DNA intermediates that can be covalently sealed by ligase (see Discussion).

A *j*-factor with units of concentration is often defined as $j = r_{\text{loop}}/r^0_{\text{dimer}}$ (4,8,13); therefore $\rho^{\text{J}}(\mathbf{0}) = (c'/c) \times j$. To calculate $\rho^{\text{J}}(\mathbf{0})$ from *j*, prior knowledge of the c'/c is needed. It is known that a nick on a linear DNA does not affect basepairing and stacking at the nicked site; therefore, hybridized DNA ends in dimerized linear DNA are in parallel and twist-matching to each other to form the *B*-DNA conformation (14,15). Hereafter we refer to this constraint as "twist-matching parallel boundary condition", denoted by Ω (Fig. 1). This results in $c'/c = (4\pi \times 2\pi)^{-1}$, where 4π arises from the constraint for tangential parallel alignment, while 2π comes from twist matching for the dimerization reaction and thus results in $\rho^{\text{J}}(\mathbf{0}) = j/(8\pi^2)$.

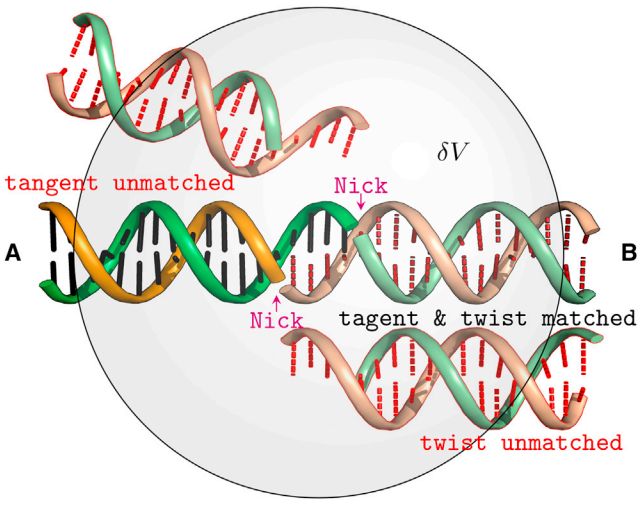

FIGURE 1 Ω-boundary condition in *j*-factor measurements. In ligase-based DNA looping experiments, within the infinitesimal volume, δV, around reference *A* end (with solid basepairing), only a subset of entered complimentary *B* ends (with dashed basepairing) can assemble into transiently stabilized hybridized *A*-*B* ends, and chemically trapped by a subsequent ligation reaction. Under the Ω-boundary condition, it entails a $(4\pi \times 2\pi)^{-1}$ factor. Tangent unmatched (*top*) and twist unmatched (*bottom*) fragments, *B* ends are shown for comparison. Note that two preexisting nicks (*arrows*) are formed immediately after hybridization, which may cause a violation of Ω-boundary condition when DNA is sharply bent. To see this figure in color, go online.

To draw information of the elasticity of DNA bending from the measured DNA looping probability density in these *j*-factor measurements, $\rho^{\text{J}}(\mathbf{0})$ can be compared with the theoretical looping probability density $\rho_{\xi}^{\text{WLC}}(\mathbf{0})$. This is based on the WLC model according to an appropriate constraint (ξ), on the orientations of the two ends in the looped DNA. In previous studies, ξ has been assumed to be Ω, which is the same as that imposed on dimerized DNA. Based on $\rho_{\Omega}^{\text{WLC}}(\mathbf{0}) = \rho^{\text{J}}(\mathbf{0})$, the DNA persistence length was determined to be in the range of 45–55 nm, over a wide contour length (>200 bp) in normal solution conditions (12,16). The agreement of the persistence length *A* determined in *j*-factor measurements and that determined in single-DNA stretching experiments validates the Ω-boundary condition for both looped and dimerized DNA with sizes larger than 200 bp.

However, for shorter DNA fragments at ~100 bp, $\rho^{\text{J}}(\mathbf{0})$ is several orders of magnitude larger than $\rho_{\Omega}^{\text{WLC}}(\mathbf{0})$ predicted with $A \approx 50$ nm (8,17). There are two possible causes of such discrepancy: 1) an intrinsic elastic response of double-stranded DNA (dsDNA) under sharp bending condition might occur by bending-induced flexible defects excited inside the DNA as proposed by several groups (8,18–21); and 2) the Ω-boundary condition assumption is no longer valid for the hybridized looped DNA when DNA is sharply bent. Violation of the Ω-boundary condition assumption could occur if the nicked sites on two hybridized ends on a sharply bent DNA loop could not maintain the *B*-form conformation. This possibility has not been considered to interpret the apparent disagreement between $\rho^{\text{J}}(\mathbf{0})$ and $\rho_{\Omega}^{\text{WLC}}(\mathbf{0})$ in previous *j*-factor studies.

Single-molecule Förster resonance energy transfer experiments

The mechanical anomaly of sharply bent DNA was also reported in two recent studies that employed single-molecule Förster resonance energy transfer (smFRET) (9,22). In these studies, complimentary ssDNA overhangs at each end of a short DNA fragment were used to stabilize the looped conformation to achieve a sufficiently long lifetime needed for smFRET measurements. Therefore, this looped DNA contained two nicks, which is similar to the looped DNA in the *j*-factor measurement before the ligation reactions.

In the first study, the looping probability was determined as a measure of the lifetimes of the looped and unlooped DNA (9). Similar to the *j*-factor measurement, an anomalously high looping probability was observed for DNA at ~100 bp compared to that predicted with the WLC model using the Ω-boundary condition. In the second study (22), the relationship of loop lifetime and the bending stress analyzed in Ω-boundary condition also revealed anomalous DNA bending elasticity for DNA fragments <100 bp (22). However, considering the presence of nicks in the hybridized DNA loops, these experiments could also be explained

by a violation of the Ω-boundary condition at the nicked sites.

In summary of these DNA looping experiments, the DNA contained preexisting nicks. It is generally assumed that nicks do not affect the local mechanical properties of sharply bent DNA, thus the observed mechanical anomaly can be explained by a breakdown of the WLC polymer model. Indeed, it has been theoretically predicted that excitation of flexible mechanical defects under bending constraints by way of DNA melting or kinking can explain these results (18–20). On the other hand, as we mentioned, the mechanical anomaly of sharply bent DNA could also be explained by violation of the Ω-boundary condition at the nicked sites.

The potential role of nicks in the DNA looping assays was only mentioned as a possible cause of the apparent DNA mechanical anomaly (23,24); however, whether a nick can promote excitation of a mechanical defect at the nicked site has never been quantitatively investigated. Under sharp bending constraints, it is possible that the nicked site might unstack, causing the formation of a flexible defect that reduces the overall bending energy of the looped DNA. As such, defect excitation would not occur in the nick-free region of DNA due to the relaxed bending in the nick-free region because of flexible defect excitation at the nicks.

In this work, we carried out full-atom MD simulations to investigate the mechanical responses of short dsDNA fragment (20 bp) under compressive load in the absence and presence of a nick in the DNA (see Materials and Methods for details on DNA constructs, spring constraints, and MD simulations).

We show that sharp DNA bending that is induced using sufficiently stiff springs with zero equilibrium length leads to local DNA basepair disruptions. Subsequently, DNA kinks with large bending angles develop around the disrupted DNA basepairs, which relaxes the bending of the rest of DNA. We also demonstrate that a nick is a structurally weaker point than basepairs in a nick-free DNA region. Thus, under sharp bending conditions nicks often lead to unstacked (basepairs intact) or peeled (basepair-disrupted) DNA, resulting in DNA kink formation localized to the nicked site. Furthermore, this nick-dependent defect excitation is sensitive to temperature changes within a physiological range.

In summary, nicks promote flexible defect excitation under sharp bending constraints, resulting in the formation of a DNA kink localized at the nicked site, which in turn prevents defect excitation in the nick-free DNA region. Based on these results, we suggest that the previously reported mechanical anomaly of sharply bent DNA can alternatively be explained as being attributable to nick-dependent flexible defect excitation.

In the Materials and Methods, we provide concise information about: 1) DNA constructs; 2) spring constraints for generating sharp DNA bending and for umbrella sampling analysis; and 3) force-field, water model, software, and other simulation aspects. In the Results, we show what is obtained on sharply bent nick-free DNA. We then present the free energy landscape and the force needed to maintain certain end-to-end distance obtained using umbrella sampling, for nick-free DNA before and after disruptions of basepairs. We also present the results of the nick-dependent defect excitation in sharply bent nick-containing DNA. In the Discussion, we provide the implications of these findings in relation to the reported anomalous DNA bending elasticity of sharply bent DNA molecules.

MATERIALS AND METHODS

DNA constructs

The 20 bp DNA sequence, Eq. 1, used in MD simulations was extracted from the 94 bp E6-94 DNA sequence used in the previous DNA cyclization experiment (8),

$$\begin{array}{l} 5' - GTGCGCACGAAATGCTATGC - 3' \\ 3' - CACGCGTGCTTTACGATACG - 5'. \end{array} \quad (1)$$

The basepairs are indexed by i, in the 5′ to 3′ direction of the top strand (also referred to as "Strand I") of the dsDNA segment. Smoothly bent *B*-form DNA were generated by the program X3DNA (25) and served as the initial conformations for the simulations (Fig. S1 in the Supporting Material). A nick on nick-containing DNA of the same sequence was generated by deleting the phosphate group on one strand between two adjacent basepairs straddling the nicked site, thus leaving the two broken backbone ends hydrolyzed (Fig. S2).

Spring constraints

Contractile springs with various equilibrium lengths/spring constants are connected between the two nitrogenous bases of the second basepair and those of the 19th basepair to induce bending of different levels. Force is distributed among their base atoms according to atomic weights. A particular spring constraint is denoted by $\{\kappa;l\}$, where κ is the spring constant in units of pN/nm and l is the equilibrium length of the spring in units of nanometers.

Two different types of simulations were performed with two different purposes. One set of simulations produced a sharply bent DNA to examine defect excitation and test if the defect causes the sharp DNA bending. For this purpose, we used springs of zero equilibrium length, adjusting their spring constants to generate forces greater than the buckling transition force to bend the DNA, yet small enough to provide sufficient time to observe both defect excitation and the development of DNA bending.

The other set of simulations scanned the free energy landscape of DNA before and after defect excitation based on umbrella sampling. Springs with finite equilibrium lengths were used to constrain the end-to-end distance fluctuations near a series of targeted values. The spring constant was determined to be sufficiently stiff to constrain the regional fluctuations, yet soft enough to allow overlapping of regional fluctuations that is needed for umbrella sampling. Because of the need to constrain the narrow regional fluctuations, these simulations are much stiffer than the first set of simulations.

MD simulations

The DNA was placed in 150 mM NaCl solution using explicit TIP3P water model (26) (see Supporting Methods in the Supporting Material). The MD

simulations were then performed using GROMACS version 4.5.5 (27–29) under recent Parm99 force field with ParmBSC0 corrections (30,31). MD simulations are usually 70 ns each consisting of 50 ns equilibration stage and 20 ns production stage. These simulations were executed using periodic boundary conditions under NVT ensemble with a constant volume of ~1170 nm^3 and a constant temperature of 300 K (or 290, 310 K with investigations into the effects of temperature). The conformational representatives during the production stage were used for extracting interested ensemble averages, such as the averages of end-to-end distances, $\langle d \rangle$. Before any constrained simulations, an unconstrained simulation of 20 bp DNA was conducted for 70 ns as control during which DNA maintained a regular helical structure with expected helical repeat and pitch (Fig. S3).

Macroscopic configuration information of DNA was extrapolated using local basepair coordinates with the x and y directions in the basepair plane and the z direction perpendicular to the basepair plane (see Fig. S4 and Supporting Methods in the Supporting Material for details). For example, the bending angle between ith and $(i + \Delta)$th basepairs, defined by $\theta_{i,i+\Delta} = \cos^{-1}(\hat{z}_i \cdot \hat{z}_{i+\Delta})$, where $i = 2, 3, \bullet\bullet\bullet, 19 - \Delta$ can be calculated for any instantaneous conformation of DNA.

RESULTS

DNA bending responses under weak and strong spring constraints

At a temperature of 300 K, a 20 bp DNA segment was forced to bend connecting to the second and 19th basepairs of the DNA with a spring of zero equilibrium length (i.e., $\{\kappa;0\}$; see Fig. S1 for initial DNA structure). Therefore, the region of DNA subject to the spring constraint has 18 basepairs and 17 basepair steps. A total of 280 DNA conformations were obtained in 14 independent simulations under various spring constraints in the range of $\kappa \in (8.0, 85.0)$ pN/nm from 50 to 70 ns at regular 1 ns intervals (Fig. 2). During each simulation, the constrained distance $d_{\{\kappa;0\}}$ between the center-of-mass of the atom groups in the two connected bases was monitored. In addition, within each DNA basepairs the interdistances of atoms involved in hydrogen-bond formation, $h_{i,j}$ (i denotes the basepair index and j denotes the jth hydrogen bond in that basepair), were also monitored.

FIGURE 2 Overview of distinctive DNA bending behaviors under weak and strong spring constraints $\{\kappa;0\}$. Above figure shows superimpositions of DNA helical axes collected per ns in last 20 ns for each simulation. The 14 independent MD simulations were all initiated from same initial (represented by *thick-red helical axis*; atomic structure is in Fig. S1), and their corresponding stabilized centerlines are represented (*light cyan*) for weak spring constants $\kappa = 8.3$, 16.6 pN/nm, and (*dark copper*) for strong bending $\kappa = 26.6$, 28.2 (five times), 29.0, 31.5, 3.2, 41.5, 49.8, and 83.0 pN/nm. When $\kappa < 20.0$ pN/nm, the centerlines are uniformly bent and more straight than the initial conformation. However, when $\kappa > 25.0$ pN/nm, the centerlines are nonuniformly bent and more curved. Note that least curved backbones from unconstrained simulations with $\kappa = 0$ pN/nm are also included for comparison.

Two representative snapshots of conformations at $t = 60$ ns during simulations confined by a weaker spring ($\kappa = 16.6$ pN/nm) and a stronger spring ($\kappa > 28.2$ pN/nm) reveal completely different bending responses (Fig. 3, *A* and *C*). The DNA under the constraint of the stronger spring assumes a much more severely bent conformation than DNA under the weaker spring, which contains disrupted basepairs highlighted with the red shadowed area. The backbones of the 280 DNA conformations can be classified into two distinctive groups based on the level of bending (Fig. 2, obtained from 14 independent simulations conducted with a wide range of spring constraints). In the weakly bent group obtained at $\kappa < 20.0$ pN/nm, the end-to-end distances of DNA are longer than that of the initial DNA (*red line*), indicating a balance between the spring elastic energy and the DNA bending energy, which relaxed DNA to a more straight conformation. In the sharply bent group obtained at $\kappa > 25.0$ pN/nm, the end-to-end distances are significantly shorter than that of the initial DNA. This indicates that the stiff springs out-competed the DNA bending elasticity and forced DNA to collapse utile the two ends collided into each other, which was accompanied with disruptions of DNA basepairs (e.g., the *shadowed region* in Fig. 3 *C*).

We investigated the weakly bent DNA under $\kappa = 16.6$ pN/nm for its structural details. The final value of $\langle d_{\{\kappa;0\}} \rangle$, which was averaged over the last 20 ns data out of 70 ns simulation, was ~4.65 nm. This is slightly longer than the initial value $d_{\text{ini}} \approx 4.20$ nm indicating the tendency of DNA to relax to a more straight conformation. However, $\langle d_{\{\kappa;0\}} \rangle$ is still slightly shorter than the expected contour length of *B*-DNA of 17 basepair steps (~5.43 nm), indicating a weakly bent conformation due to this spring constraint. The minimal and maximal lengths of hydrogen bonds in each weakly bent basepair, which were averaged in the last 20 ns, $\langle \min(h_{i,j}) \rangle$ and $\langle \max(h_{i,j}) \rangle$ completely overlap with those of control ($\kappa = 0$ pN/nm). This indicates that the weakly bent DNA remained intact throughout 70 ns simulation (Fig. 3 *B*). The hydrogen-bond length fluctuates within 0.26–0.33 nm with an average value ~0.30 nm, which is consistent with hydrogen-bond lengths in the crystal structures of *B*-form DNA (32). Thus, hereafter a basepair is considered as Watson-Crick basepair when all its hydrogen-bond lengths are <0.33 nm.

On the other hand, the *B*-DNA became unstable when $\kappa > 25.0$ pN/nm, resulting in sharply bent DNA conformations with very short final $\langle d_{\{\kappa;0\}} \rangle < 2.30$ nm (Fig. S5). Considering volume exclusion, this suggests that only a distance of DNA diameter separates the two DNA ends. Such sharp DNA bending is always accompanied with disruption of DNA basepairs. As an example, the conformation

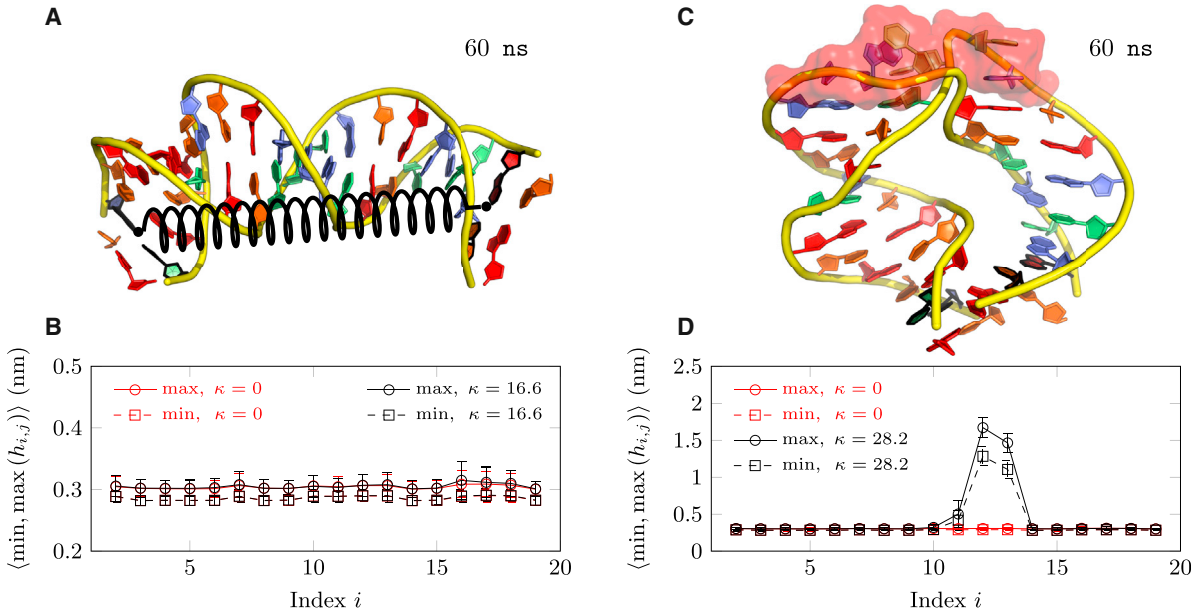

FIGURE 3 Different DNA bending responses under weak and strong spring constraints {κ;0}. (*A*) A snapshot of a smoothly bent DNA conformation at $t = 60$ ns under a weak spring constant $\kappa = 16.6$ pN/nm. (*B*) Corresponding hydrogen-bonding profile, $\langle \min, \max(h_{i,j}) \rangle$ plotted against i values ($i = 2, 3, \cdots, 19$) averaged from the last 20 of 70 ns simulation. (*C*) A snapshot of a severely bent DNA conformation at 60 ns under a strong spring constant $\kappa = 28.2$ pN/nm, which contains a local basepair disruption in the middle. (*D*) $\langle \min, \max(h_{i,j}) \rangle$ averaged over the last 20 ns reveals three disrupted basepairs at $i = 11$, 12, 13, which are highlighted with the red surfaces in (*C*).

snapshot at 60 ns of a simulation with $\kappa = 28.2$ pN/nm contains a localized sharp bend near the middle of the DNA (Fig. 3 *C*). The hydrogen-bonding profile, $\langle \min, \max(h_{i,j}) \rangle$, of this sharply bent DNA (Fig. 3 *D*) clearly indicates that the 11th–13th basepairs are disrupted.

Basepair disruption results in localized sharp DNA bending

We then sought to analyze the influence of local DNA basepair disruption in sharply bent DNA on the overall shape of DNA. Thus, we calculated the bending angle between the intact 10th and 14th basepairs that straddles the disrupted region of DNA bent under $\kappa = 28.2$ pN/nm using $\theta_{10,14} = \cos^{-1}(\hat{z}_{10} \cdot \hat{z}_{14})$, where $\hat{z}_i$ describes the direction perpendicular to the ith basepair plane (see Materials and Methods and Fig. S4 for details). The first row in Fig. 4 shows that evolution of $\theta_{10,14}$ from initial ~40° toward larger bending angle began immediately after the simulation started. Saturated local bending was reached within 10 ns, and remained at a high bending level at ~160° throughout the remainder of the simulation.

We also plotted the evolutions of bending angles of two unaffected regions of the same length ($\theta_{6,10}$ and $\theta_{14,18}$, *row 1* of Fig. 4). Synchronized with DNA kink formation of $\theta_{10,14}$, these bending angles relaxed from initial ~40° to values of ~30° and ~10° within 10 ns, respectively, and remained at these low bending levels throughout the remainder of the simulation. These results indicate the kink formation relaxes the rest of the DNA to a more straight conformation.

We further examined the correlation between the localized kink formation and the disruption of basepairs. Time traces of $h_{i,j}$ for the three affected A=T basepairs $i = 11$, 12, 13 are shown in rows 2–4 of Fig. 4. These results reveal

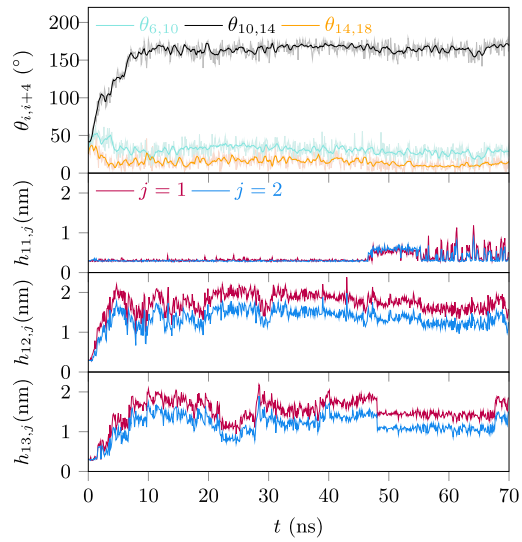

FIGURE 4 The dynamics of local bending deformations and hydrogen-bond disruptions under {κ;0} with $\kappa = 28.2$ pN/nm over 70 ns. (*Row 1*) Evolution of $\theta_{10,14}$ enclosing three basepairs at $i = 11$, 12, 13 disrupted during the simulation shows that kink development around the region with disrupted DNA basepairs. The bending angle evolution of two intact regions with same length, $\theta_{6,10}$ and $\theta_{14,18}$, is shown for comparison. (*Rows 2–4*) Evolution of $h_{i,j}$ for the three disrupted basepairs $i = 11$, 12, 13, which are all A=T basepairs and involve two atom-atom distances each ($j = 1$ and $j = 2$). To see this figure in color, go online.

that the 11th basepair remained intact in the first ~48 ns, and was then disrupted between ~48 and 56 ns, after which it fluctuated between disrupted and intact states. The 12th and 13th basepairs opened up within 10 ns and remained disrupted. Clearly, DNA kink formation and disruptions of these basepairs are highly correlated. Hence, we conclude that basepair disruption causes kink development. We also note that sharply bent DNA containing disrupted basepairs could be restored into a straight *B*-form DNA conformation within 50 ns upon removal of the spring constraint from the DNA (Fig. S6).

Central localization of defects

The development of similar localized kinks was observed in all 12 independent simulations using $\kappa > 25.0$ pN/nm, which was accompanied with basepair disruptions at kinked locations. These kinks primarily located around the same region near the center, are likely due to the high curvature at the center under our bending geometry.

Fig. 5 *A* plots the hydrogen-bonding profiles, $\langle \min, \max(h_{i,j})\rangle$ against i values averaged over the last 20 ns (from all 12 independent simulations with $\kappa > 25.0$ pN/nm). This plot reveals that the disrupted basepairs occur around the same region near DNA center that are AT-rich (i.e., 5′–AAAT–3′, the 10th–13th basepairs). One possible cause for the central localization of basepair disruption is that the largest curvature occurs at the center (Fig. S7). Alternatively, it may be due to the less stable noncovalent interactions of AT-rich region in the middle of our DNA. Based on the unified NN basepair parameters by SantaLucia (33), melting A=T next to A=T basepairs is more feasible energetically than melting A=T next to G≡C or melting G≡C next to A=T basepairs, and melting G≡C next G≡C basepairs is the hardest.

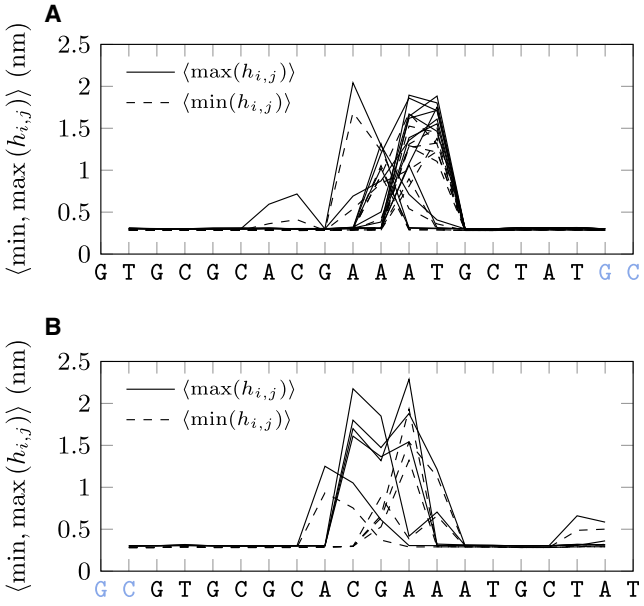

FIGURE 5 Central localization of defects on different sequences. Hydrogen-bonding profiles of DNA containing disrupted DNA basepairs: original sequence 5′–*GTGCGCACGAAATGCTATGC*–3′ and modified sequence 5′–*GCGTGCGCACGAAATGCTAT*–3′. Overlay of $\langle \min(h_{i,j})\rangle$ (*dashed lines*) and ($\langle \max(h_{i,j})\rangle$, *solid lines*) along the DNA sequence, averaged over the last 20 ns for (*A*) 12 independent simulations with the original sequence and (*B*) five independent simulations with the modified sequence. All the hydrogen-bonding profiles were obtained through constrained simulations ($\{\kappa;0\}$), with various $\kappa > 25.0$ pN/nm (i.e., $\kappa = 26.6$, 28.2 (five times), 29.0, 31.5, 33.2, 41.5, 49.8, and 83.0 pN/nm for the original sequence; whereas $\kappa = 28.2$, 31.5, 33.2, 41.5, and 49.8 pN/nm for the modified sequence). The modified sequence was generated from the original sequence by removing the tailing 5′–*GC*–3′ and inserting it at the front, which offset the AT-rich region (i.e., its 10th–13th basepairs) away from its center. To see this figure in color, go online.

To see which factor predominates in central localization, we shifted the entire sequence tail-to-head by 2 bp and replaced the central AT-rich island at the 10th–13th basepairs with 5′–CGAA–3′. Five independent simulations under different level of strong bending using $\{\kappa;0\}$ spring constraints with $\kappa > 25.0$ pN/nm were conducted for 70 ns. The overlay of the resulting hydrogen-bonding profiles in Fig. 5 *B* shows that basepair disruptions still occurred at the central region, mainly at the 10th–11th basepairs (i.e., G≡C basepairing), and 12th basepairs (i.e., A=T basepairing). Taken together, these results suggest that the central localization of the basepair disruptions is mainly caused by the high curvature at the center of DNA, while the sequence effects are minimal under our bending constraints.

DNA conformational free energy and force distance curves

To understand the mechanics of DNA under bending, we calculated the DNA conformational free energy as a function of end-to-end distance, $\mathcal{A}(d)$, as well as the force required to maintain an end-to-end distance, $f(d)$, using umbrella sampling for DNA under 12 different spring constraints $\{248.9;\ l_m\}$ indexed by m. Here, a fixed stiff spring constant of $\kappa = 248.9$ pN/nm was used in all simulations to ensure that the end-to-end distance of DNA fluctuates near the equilibrium spring length of l_m. A series of l_m values (5.27, 5.18, 4.94, 4.79, 4.56, 4.31, 4.17, 4.16, 3.80, 3.37, 3.01, and 2.85 nm) where $l_1 > l_2 > \cdots > l_{12}$ were used to produce different levels of bending constraint. The global unbiased $\mathcal{A}(d)$ was then obtained based on these constrained local fluctuations using the standard weighted histogram analysis method g_wham (34,35) (see details in the Supporting Methods in the Supporting Material).

The 12 constrained simulations led to nine segments with intact DNA basepairs ($m = 1, 2, \cdots, 9$) and three segments containing disrupted basepairs in the region of 11th–13th basepairs ($m = 10,11,12$) in the last 20 ns of total 50 ns simulations. The inset of Fig. 6 shows $\mathcal{A}(d)$ of *B*-form DNA obtained from nine intact DNA simulations (*dark-red solid line*), which contains a single energy minimum (set as 0 k_BT) at $d_e \approx 5.43$ nm. A DNA rise of ~0.32 nm/bp

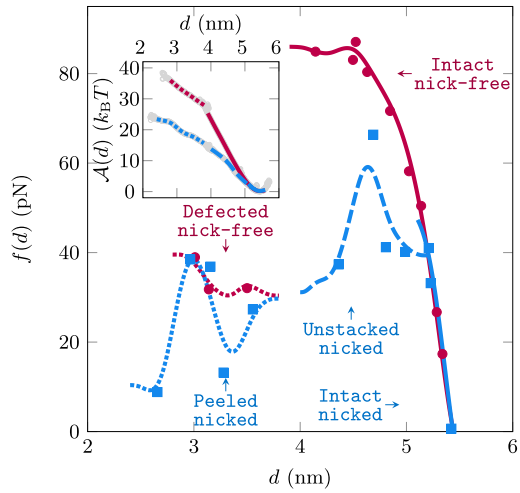

FIGURE 6 The $\mathcal{A}(d)$ and $f(d)$ obtained for various types of DNA at 300 K. (*Inset*) Smoothed $\mathcal{A}(d)$, reference to global minimum state, for intact nick-free DNA (*dark-red solid line*), defect-containing nick-free DNA (*dark-red dotted line*), intact nicked DNA (*light-blue solid line*), unstacked nicked DNA (*light-blue dashed line*), and peeled nicked DNA (*light-blue dotted line*). Main figure shows $f(d) = -\partial\mathcal{A}(d)/\partial d$ for different types of DNA again were represented by different colors and line styles: intact nick-free DNA (*dark-red solid line*), defect-containing nick-free DNA (*dark-red dotted line*), intact nicked DNA (*light-blue solid line*), unstacked nicked DNA (*light-blue dashed line*), and peeled nicked DNA (*light-blue dotted line*). For each type of DNA in the main figure, the force values were directly read from the spring as well, which are indicated by corresponding dots for nick-free DNA and corresponding squares for nicked DNA. (*Inset*, *gray circles*) Discrete data obtained from WHAM umbrella sampling analysis that were used to produce continuous $\mathcal{A}(d)$ by cubic spline interpolation.

estimated by $d_e/17$ is consistent with expected DNA rise of 0.33 ± 0.02 nm/bp in the *B*-form DNA duplex (36). Note that there are 17 basepair steps between the two spring-connected basepairs. We also obtained the $\mathcal{A}(d)$ for defect-containing DNA (*dark-red dotted line*, obtained with three simulations of DNA with disrupted basepairs), which appears to have a smaller slope than the $\mathcal{A}(d)$ of *B*-form DNA. Because the umbrella sampling analysis was performed separately for the each type of DNA, the $\mathcal{A}(d)$ profiles have an undetermined offset from each other. Upon shifting the $\mathcal{A}(d)$ of defect-containing DNA to match that of *B*-form DNA at their overlapping region, we noted that this shift does not affect the calculation of $f(d)$.

A continuous force-distance curve could be obtained by $f(d) = -\partial\mathcal{A}(d)/\partial d$. The $f(d)$ of *B*-form DNA is shown in Fig. 6 (*dark-red solid line*). This curve overlaps with results obtained by a direct readout through $f(\langle d_{\{\kappa;l_m\}}\rangle) = \kappa \times (\langle d_{\{\kappa;l_m\}}\rangle - l_m)$, where $\langle d_{\{\kappa;l_m\}}\rangle$ is the average end-to-end distance under a particular spring constraint $\{248.9; l_m\}$ (corresponding *dark-red dots*). As expected, at the equilibrium distance $d_e \approx 5.43$ nm, the $f(d_e) = 0$ pN. When d is slightly shorter than d_e, the $f(d)$ increases linearly as d decreases. The axial Young's modulus of DNA is estimated to be $Y = (\Delta f/\Delta d)(L/S) \approx 300$ pN/nm^2 as a result of this linear stress-strain relation (with the contour length $L \approx d_e$, cross section $S = \pi R^2$, and radius $R = 1.0$ nm). The bending persistence length is estimated to be $A = \beta YI \approx 57.0$ nm, which is close to 53.4 ± 2.3 nm previous determined in single-DNA stretching experiments (37).

A transition from the initial linear force-distance curve ($d > 4.80$ nm) to a nearly flattened profile ($4.00 < d < 4.60$ nm) occurs during decreasing d in conditions where $4.80 > d > 4.60$ nm, which corresponds to a force range of 70–85 pN. This behavior can be explained by the classical Euler buckling instability of elastic rods. Here, $f_c = \beta^{-1}\pi^2 A/L^2$ predicts a critical force at the onset of the rod bending (i.e., buckling transition), when $L << A$, where A is bending persistence length, and L is DNA contour length. Using the simulated $A \approx 57.0$ nm, the f_c value is estimated to be 79.1 pN, which is in agreement with the simulated force range. Thus, we have successfully predicted the Young's modulus and the buckling transition force of *B*-form DNA, which indicates that the force field is suitable for simulating large-scale DNA mechanical properties. The result also indicates that the overall shape of DNA has reached equilibrium over a wide range of bending constraints within our simulation time.

Similar simulation constrained by $\{248.9; l_m\}$ was also performed for defect-containing DNA. The $f(d)$ obtained by $-\partial\mathcal{A}(d)/\partial d$ (Fig. 6, *dark-red dotted line*) as well as with a direct readout (corresponding *dark red dots*) are also in agreement with each other. These results reveal a significantly decreased $f(d)$ by ~50 pN compared to *B*-DNA force plateau after the buckling transition, indicating that the defect-containing DNA is more flexible. In comparison to *B*-DNA, $f(d)$ obtained for the defect-containing DNA has a more rugged profile. This is because the defect-containing DNA does not have well-defined structures due to different types of defects and varying levels of transient stacking with nearby basepairs.

Effects of nick on the micromechanics of sharply bent DNA

To obtain insights into the experimental mechanical anomaly of sharply bent DNA that contained nicks, we investigated the effects of nick on the micromechanics of sharply bent DNA. We first performed MD simulations constrained by a zero-length spring with $\kappa = 28.2$ pN/nm (i.e., spring constraint of {28.2; 0} to generate sharply bent conformations for four DNA segments containing a single nick at different locations along the top strand (Fig. S2, nicks between the 6th and 7th, between the 8th and 9th, between the 11th and 12th, and between the 13th and 14th basepairs, explicitly). During simulations, the interbase distances between the adjacent C4′ atoms along the sugar-phosphate backbone of the nicked strand, $\delta_{i,i+1}$, were

monitored. Here i is the basepair index, which indicates the numbering of C4′ atoms starting from the first basepair.

For each of the four nicked DNAs, sharp bending led to significantly increased $\delta_{i,i+1}$ that straddles the nick, indicating separation of the two nick-straddling C4′ atoms and their associated bases (Fig. 7). The separation of the two C4′ atoms is either caused by strand separation involving a few melted basepairs near the nick (hereafter referred to as "peeled") or by unstacked basepairs straddling the nick without hydrogen-bond disruptions (hereafter referred to as "unstacked") (Figs. S8 and S9). The selection between the two types of defects depends on the two nick-straddling basepairs, where G≡C basepairs are prone to unstacked defects and A=T basepairs are prone to peeled defects (Fig. S10).

Further analysis shows that the separation of the two C4′ atoms straddling the nick is accompanied with a large bending angle developed at the nicked position, which in turn relaxes the rest of DNA into a less bent *B*-form conformation. An example of this basepair separation is shown in Fig. 8 *A*, where the nick is located between the 8th and 9th basepairs. In the sharply bent conformation, the 8th and 9th basepairs were unstacked, leading to the increased $\delta_{8,9}$. The bending angle between the 7th and 10th basepairs, $\theta_{7,10}$, rapidly increased from the initial value of ~30° to ~150° within 2 ns after simulation began, and synchronized with the increase in $\delta_{8,9}$. It also synchronized with relaxations of the three-basepair step bending angles in the rest of DNA to more straight conformations, as shown by the evolution of $\theta_{4,7}$ and $\theta_{10,13}$. In another example, a similar nick between the 11th and 12th basepairs promoted local sharp bending in the case of strand separation around the nick (i.e., peeling) (Fig. 8 *B*). This peeling was caused by disruptions of hydrogen bonds in the adjacent 11th, 10th, and 9th basepairs. The development of a large bending angle around the nicked position synchronized with the relaxation of the rest of DNA to a less bent *B*-form conformation as well.

Then, using {248.9; l_m}-constrained simulations with umbrella sampling analysis similar to those used with nick-free DNA, we obtained the free energy-distance ($\mathcal{A}(d)$) and force-distance ($f(d)$) profiles for DNA containing a nick between the 11th and 12th basepairs (Fig. 6, *light blue lines*). Both profiles overlap with the intact nick-free DNA under weak bending conditions, suggesting that the nicked DNA assumes *B*-form at the nicked sites and has similar bending elasticity to nick-free DNA under weak bending conditions. However, increased bending leads to deviation of the profiles from the *B*-form profiles due to unstacking of the 11th and 12th basepairs, which occurs between 4.00 and 5.20 nm. Further bending ($d < 4.00$ nm) causes the peeling of 1–3 bp of nearby basepairs. The unstacking and peeling occurring at $d < 5.20$ nm results in a force plateau of <40 pN, which is significantly smaller than the buckling transition force of *B*-form DNA (~80 pN). After the flexible defect was excited at the nicked site, the $f(d)$ becomes rugged, which is similar to the profile observed for nick-free DNA with basepair disruptions excited inside. Overall, these results demonstrate a nick-dependent DNA softening through nick-promoted excitations of flexible defects.

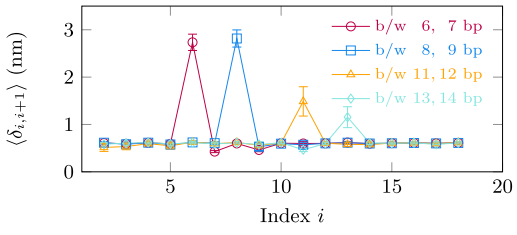

FIGURE 7 Interbase distance profiles for the four nicked DNAs under a spring constraint of {28.2; 0}. The interbase distance profiles, $\langle \delta_{i,i+1} \rangle$ ($i = 2, 3, \cdots, 18$) measure the averaged distances between adjacent C4′ atoms of ith and ($i + 1$)th basepairs on the entire top strand of DNAs in the four independent simulations with nick right after the 6th, 8th, 11th, and 13th basepairs. The dramatic increase in $\langle \delta_{i,i+1} \rangle$ in the corresponding nick-containing simulations reveals that disruptions of basepairs occurred at nicked sites. Note that C4′ atoms of deoxyribose are part of the DNA sugar-phosphate backbone. To see this figure in color, go online.

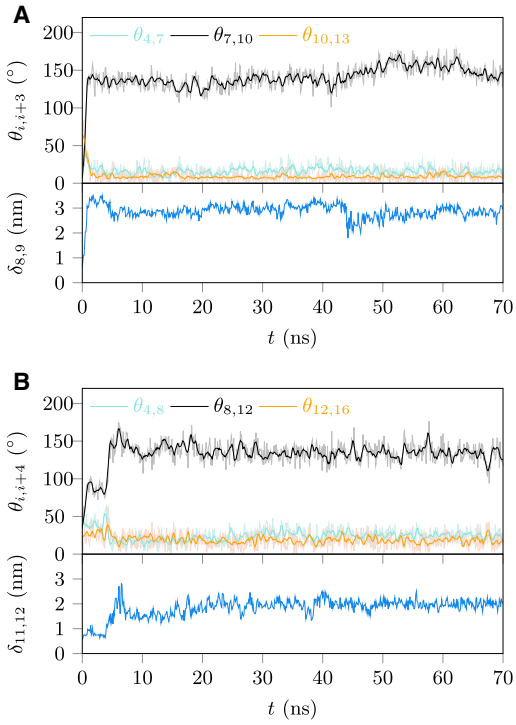

FIGURE 8 The dynamics of local bending deformations and basepair separations at nicked sites under a spring constraint of {28.2; 0} over 70 ns. (*A*) (*Row 1*) Evolution of $\theta_{7,10}$, enclosing the nicked site between the eighth and ninth basepairs, which shows kink development around the unstacked region. The bending angle evolution of two intact regions with same length, $\theta_{4,7}$ and $\theta_{10,13}$, is shown for comparison. (*Row 2*) Evolution of $\delta_{8,9}$ indicates basepair separation at nicked sites. (*B*) Similar dynamics of kink development ($\theta_{8,12}$), bending relaxation ($\theta_{4,8}$; $\theta_{12,16}$), and basepair separation ($\delta_{11,12}$) for the peeled DNA with nick between 11th and 12th basepair. To see this figure in color, go online.

Effects of direction of bending on defect excitation

To understand whether the direction of bending could affect the defect excitation, we performed a series of 70 ns simulations using zero-length springs with a variety of spring constants (i.e., {κ;0}) for both nick-free and nicked DNA bent into three evenly separated directions (Fig. 9, *top view*) denoted by *i*, *ii*, and *iii*. Each initial DNA conformation has a uniform bending angle per basepair step of $\theta = 3.8^\circ$ by adjusting the tilt and roll angles of the basepairs (see values in Table S1 in the Supporting Material).

In simulations with nicked DNA, a single nick was introduced in the top strand after the 11th basepair. As shown in the side view of Fig. 9, a local polar coordinate is defined at the nicked site with the opposite-normal direction as the polar axes. In the local polar coordinate, the angular positions of the nick are $+60^\circ$, $+180^\circ$, and -60° in the DNAs bent into the directions *i*, *ii*, and *iii*, respectively. In the cases of $\pm 60^\circ$ nick positions (i.e., the bending directions *i* and *iii*), the nick is under a tensile stress; for the $+180^\circ$ nick position (i.e., the bending direction *ii*), the nick is under a compressive stress.

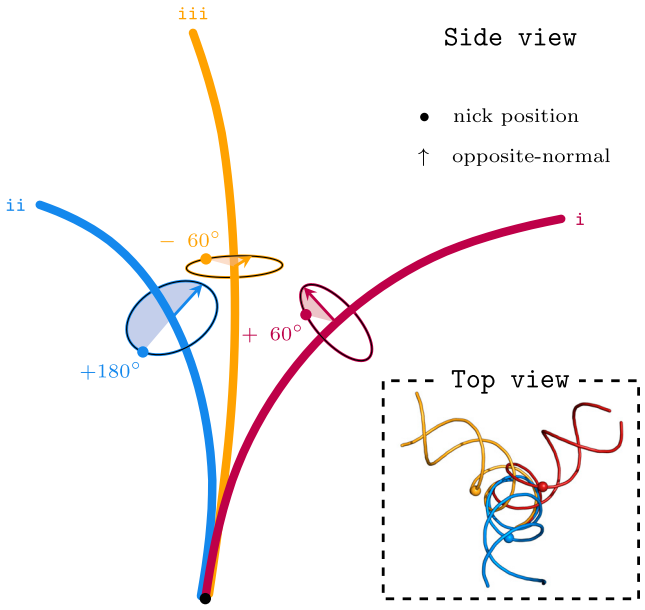

FIGURE 9 Initial conformations for nicked and nick-free DNA bent into different directions. The first basepairs are superimposed; therefore, the initial conformations have the same starting orientation. The three DNA molecules are bent uniformly outward in three distinctive directions, denoted *i*, *ii*, and *iii*, with their end-to-end distances projected onto the first basepair plane evenly separated. (*Side view*) At the particular location corresponding to where a nick is introduced, a local polar coordinate is defined with the opposite-normal direction as its polar axis indicated (*arrow*). The nick positions (*indicated with dots*) in the DNAs are $\pm 60^\circ$ and $+180^\circ$ in the corresponding local polar coordinates. (*Inset*, *top view*) The three DNA duplexes with spheres denoting the phosphate groups that are deleted in the nicked DNA on Strand I between the 11th and 12th basepairs. The initial bending is controlled by tilts and rolls of the basepairs provided in Table S1. To see this figure in color, go online.

Simulations for the nick-free DNA were conducted under two spring constraints of $\kappa = 16.6$ and 28.2 pN/nm. Under $\kappa = 16.6$ pN/nm, the *B*-form DNA conformations remained intact throughout the simulations, as demonstrated by the hydrogen-bonding profiles averaged from the last 20 ns simulations (Fig. 10 *A*, *top*). In contrast, under the stronger constraint of $\kappa = 28.2$ pN/nm, defect excitation occurred near the middle of the DNAs regardless of direction of bending (Fig. 10 *A*, *bottom*). These results suggest that for nick-free DNA, the defect excitation is not sensitive to direction of bending.

Similar simulations were performed for the nicked DNA under three spring constraints of $\kappa = 8.3$, 16.6, and 28.2 pN/nm. Under $\kappa = 8.3$ pN/nm, defect excitation was not observed in any bending direction according to their interbase distance profiles averaged in 50–70 ns (Fig. 10 *B*, *top*). However, under $\kappa = 16.6$ pN/nm, defect excitation only occurred in the bending direction *i*, which was located at the nicked site (Fig. 10 *B*, *middle*). Considering that under the same spring constant, defects cannot be excited for nick-free DNA in any bending direction, this result is consistent with our conclusion that nicks can facilitate defect excitation. In addition, because the defect excitation only occurred in one bending direction within our simulation timescale, this suggests that bending-induced nick-dependent defect excitation may have an anisotropic dependence on the direction of bending. Under the strongest constraint of $\kappa = 28.2$ pN/nm, defects were excited at the nick regardless of direction of bending (Fig. 10 *B*, *bottom*).

Overall, these results again demonstrate central localized defect excitation in sharply bent nick-free DNA, and defect excitation at nicked sites in sharply bent nick-containing DNA. In addition, a much weaker initial bending (~3.8° per basepair step) was used here compared to that in Figs. 2, 3, 4, 5, 6, 7, and 8 (~10° per basepair step), which further suggests that the main results of our simulations do not depend on the level of initial bending.

Effects of temperature on nick-dependent defect excitation

Because DNA basepair stability is sensitive to temperature and several sharp DNA bending experiments were performed with different temperatures, we investigated the effects of temperature at 290, 300, and 310 K on the nick-dependent defect excitation. For this, we used a spring with an equilibrium length of 4.20 nm and a spring constant of 248.9 pN/nm (i.e., a spring constant of {248.9; 4.20}) to bend the DNA. Four simulations were run for 50 ns at each temperature to obtain the defect excitation statistics. As defects did not occur in the nick-free DNA at these temperatures with this spring constraint (data not shown), we decided to probe the nick-dependent defect excitation at different temperatures with {248.9; 4.20}. As

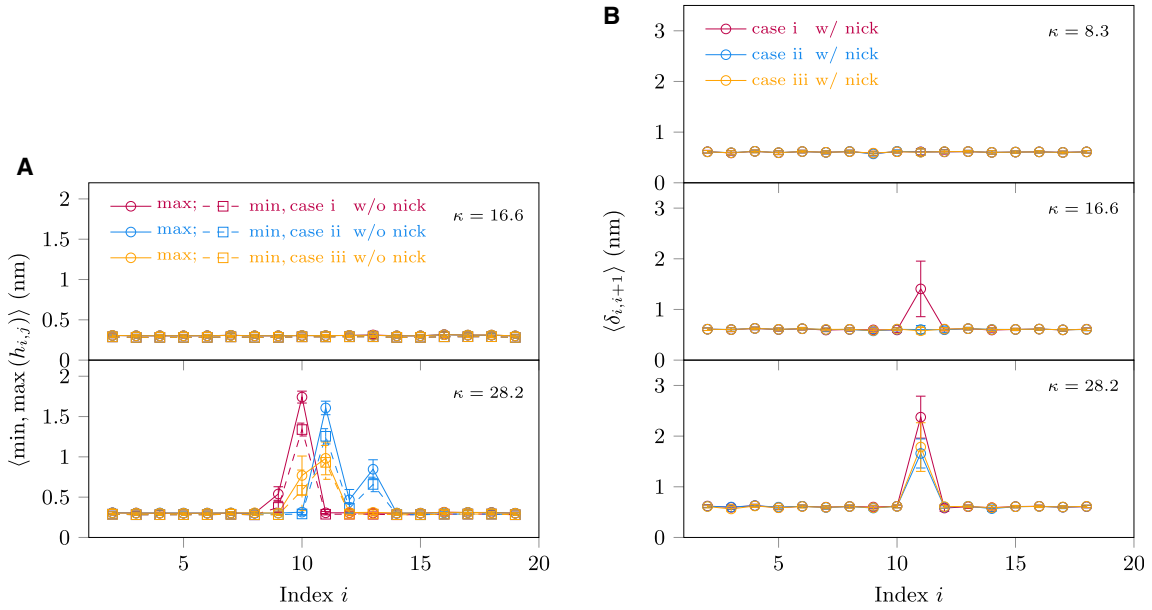

FIGURE 10 Effects of direction of bending on defect excitation in three distinct directions *i*, *ii*, and *iii*. DNA molecules without and with nicks were forcibly bent toward distinctive directions using various spring constraints of {κ;0}. (*A*) The hydrogen-bonding profiles of nick-free DNA, ($\langle\min(h_{i,j})\rangle$, *dashed lines*) and ($\langle\max(h_{i,j})\rangle$, *solid lines*) along the DNA sequence averaged in 50–70 ns trajectories for different bending directions under constraints of κ = 16.6 (*top*) and 28.2 (*bottom*) pN/nm. (*B*) Interbase distance profiles ($\langle\delta_{i,i+1}\rangle$) between adjacent C4′ atoms on Strand I for the nick-containing DNA, averaged in 50–70 ns trajectories for the three bending directions under three spring constants of κ = 8.3 (*top*), 16.6 (*middle*), and 28.2 (*bottom*) pN/nm. To see this figure in color, go online.

the nick-dependent defect excitation is likely anisotropic, we introduced three nicks located after the 8th basepair on Strand I, the 10th basepair on Strand II, and the 12th basepair on Strand I (Fig. S11 *A*). Under any bending direction, the three nicks are exposed to different bending orientations, which minimize the potential anisotropic effect. During simulations, the interbase distances along Strand I and II were monitored. They are denoted by $\delta^{\mathrm{I}}_{i,i+1}$ and $\delta^{\mathrm{II}}_{i,i+1}$, respectively.

Under such bending constraints at 290 K, defect excitation occurred at the nicks. However, the defect excited state was not the predominant form and a transient defected nick rapidly restacked (Fig. S11 *B*, *top*, obtained at 290 K). Their interbase distance profiles, $\langle\delta^{\mathrm{I,\,II}}_{i,i+1}\rangle$, for both strands are consistently similar to that of nick-free DNA (Fig. 11, *top*), further indicating that the nicked sites predominantly exist in the stacked *B*-form conformation. The main mechanical effect of this transient defect excitation is that the force in the spring to maintain such bending constraint is ~10% lower than that for nick-free control DNA (Table 1, for all four simulations at 290 K averaged in the last 20 ns).

In sharp contrast, defect excited states dominated in all simulations performed at both 300 and 310 K (see Fig. S11 *B*, *bottom*, obtained at 300 K). The interbase distance profiles significantly deviate from the *B*-form behavior at one or more nicked sites (Fig. 11, *middle* and *bottom*). Furthermore, the force required to maintain the same bending constraint is drastically reduced compared to that for nick-free DNA, and that for nicked DNA at 290 K (Table 1). Together, these results indicate that the nick-dependent flexible defect excitation is sensitive to temperature—decreasing temperature can significantly inhibit defect excitation at nicked sites.

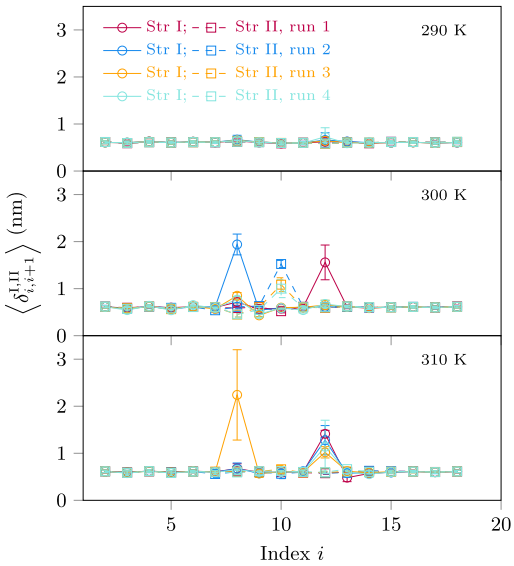

FIGURE 11 Effects of temperature on nick-dependent defect excitation. DNA molecules with triple nicks were constrained by the spring of {248.9; 4.20}. Four independent 50 ns simulations were performed for each indicated temperature. The panels show the interbase distance profiles for both strands along the DNA averaged in the last 20 ns of each simulation: $\langle\delta^{\mathrm{I}}_{i,i+1}\rangle$ (*solid*) and $\langle\delta^{\mathrm{II}}_{i,i+1}\rangle$ (*dashed*), where *i* denotes the basepair index, and superscripts I and II denote the top and bottom strands, respectively. To see this figure in color, go online.

TABLE 1 Force ($\langle \kappa \times (d_{\{248.9;\ 4.20\}} - l) \rangle$) under the spring constraint of {248.9; 4.20} at different temperatures

	Force (pN)		
	290 K	300 K	310 K
Run 1	69.9	1.5	35.6
Run 2	69.7	29.3	27.2
Run 3	67.7	12.5	16.0
Run 4	66.4	19.9	20.0
Control	81.7	83.3	82.5

The mean values of force in the spring (i.e., in units of picoNewtons) are calculated in the last 20 of 50 ns simulations for nicked DNA at three indicated temperatures, with four simulations performed at each temperature denoted by runs 1–4. For comparison, forces obtained on nick-free DNA as control are ~82 pN even at 310 K.

DISCUSSION

In this work, we observed excitation of flexible DNA defects in sharply bent DNA with disrupted basepairs. However, when the DNA contained a nick, excitation of flexible defects predominantly occurred at the nicked site. Such preferential excitation of flexible defects at nicked sites subsequently absorbed bending to nicks and relaxed the level of bending elsewhere in the DNA, which in turn suppressed defect excitation in nick-free region. These results suggest that a nick in a DNA is a structurally weaker point compared to the nick-free DNA region, which undergoes unstacking/peeling upon sharp bending. This is in agreement with results obtained in a recent coarse-grained MD simulation by Harrison et al. (38,39). The idea that a nick is a weaker structural point was also suggested by an earlier experiment showing that the unstacking/peeling transition occurred preferentially at the nicked site with increasing temperatures (40,41).

Previous *j*-factors measured for large DNA (>200 bp) are consistent with those predicted by the WLC model indicating that weakly bent DNA in large loops could maintain a *B*-form conformation at the hybridized double-nicked region, and therefore satisfy the Ω-boundary condition. This is consistent with our results showing that under weak bending, a nick remains in the stacked state with a *B*-form conformation and bending stiffness.

The *j*-factor measurements strongly deviated from the canonical WLC predictions when performed for shorter DNA fragments of 94–116 bp. While the *j*-factor was only slightly above the WLC prediction for 116 bp fragments, *j*-factors could be several orders of magnitude greater than WLC predictions with shorter fragments of DNA (8,9,17,42). The mechanics of the unexpectedly high DNA looping probability was previously explained by excitation of flexible defects inside DNA (8,9,17–20,22). Our results of the nick-dependent defect excitation in sharply bent DNA provide another highly possible explanation: unstacking/peeling excitations at the nick under increased level of bending implies violation of the Ω-boundary condition in looping experiment with short DNA fragments. As shown with previous theoretical predictions (19,23,43), if the two ends of the same DNA can meet in a kinked conformation, the looping probability density is much higher compared to that under the Ω-boundary condition. Therefore, comparison between the experimental *j*-factor measurements and theoretical predictions based on the WLC model under the Ω-boundary condition will lead to significantly overestimated DNA bending flexibility.

Here, we discuss the possibilities of violating the Ω-boundary condition in the smFRET and the ligase-based *j*-factor measurements. In the smFRET measurements, DNA looping is purely dependent on hybridization of the complementary ends. Therefore, both nicks are under bending stress and can be unstacked/peeled. The ligase-based *j*-factor measurements are more complex as the looped DNA is covalently sealed by a subsequent ligation reaction for quantification. An important question is whether the ligase enzyme only recognizes a subset of the looped DNA, thereby imposing an additional constraint on the conformation of the nicked sites. If the ligase can recognize a kinked nick and use the binding energy to deform the nick into a conformation that allows ligation, then the Ω-boundary condition can be violated due to the nick-dependent defect excitation. Furthermore, if a ligase can only recognize a stacked *B*-form nick, the Ω-boundary condition can still be violated because when a ligase seals a stacked nick in a double-nicked DNA loop, the other nick can still remain in an unsealed unstacked state, whereas the DNA loop is already irreversibly closed.

It is well known that the stacking energy between DNA basepairs has a strong dependence on temperature (33), which may be related to a discrepancy between two *j*-factor measurements for 94 bp DNA fragments. A canonical WLC elastic response of DNA was reported at 21°C (13), which is in contrast to the mechanical anomaly observed at 30°C (8,17). Our simulations at different temperatures revealed that the unstacking of the nick in a sharply bent DNA is highly sensitive to temperature, which is significantly suppressed when the temperature was reduced from 300 to 290 K. The observed trend of temperature dependency of nick-dependent defect excitation in a sharply bent DNA provides a possible explanation to the experimental discrepancy.

DNA mechanical anomaly was also reported by analyzing the elastic energy of short dsDNA fragments, which were constrained in a sharply bent conformation using a short ssDNA connecting the two dsDNA ends (44,45). However, a preexisting nick was introduced to the middle of the dsDNA in those experiments, while the interpretation of the intrinsic mechanical anomaly of dsDNA relied upon the assumption that the nick remained in the *B*-form conformation in the experiments. According to our simulation, the apparent anomaly observed in those experiments could also be explained by a nick-dependent flexible defect excitation.

The mechanics of sharply bent DNA was also studied in sharply bent nick-free DNA fragments. Shroff et al. (46) bent a nick-free 25 bp (24 basepair steps) dsDNA fragment using a 12 nt ssDNA connecting the two dsDNA ends. The work reported a tension in the ssDNA of 6 ± 5 pN, a few times smaller than the buckling transition force (~30 pN) expected from the canonical WLC model, indicating mechanical anomaly in this sharply bent DNA. As the level of bending in this experiment is much higher than that in ~100 bp DNA minicircles (see Supporting Discussion in the Supporting Material for details), it does not provide an answer to whether a similar mechanical anomaly could occur in ~100 bp nick-free DNA minicircles. Mechanical anomaly in severely sharply bent DNA can be explained by flexible defect excitation inside DNA due to basepair disruption. It is consistent with our simulations on nick-free DNA and an experiment reporting ssDNA formation in covalently ligated 63–65 bp DNA minicircles based on BAL-31 nuclease digestion assay (47,48).

Deviation from the canonical WLC model was also reported based on analyzing the bending angle distribution over short DNA contour length using atomic force microscopy imaging in air. That study reported that 5–10 nm DNA fragments have a significantly higher probability for larger bending angle than that predicted by the canonical WLC polymer model (49). However, one cannot exclude the possibility that perturbation during sample drying processes might cause rare large DNA kinks. Indeed, this has been demonstrated in a more recent atomic force microscopy imaging experiment carried out in solution, which reported a normal bending angle distribution expected from the canonical WLC polymer model for ~10 nm DNA fragments (50).

The micromechanics of DNA bending was also studied by analyzing the shapes of 94 bp DNA minicircles imaged using cryo-electron microscopy for three DNA constructs: 1) DNA contains two 2 nt ssDNA gaps, 2) DNA contains two nicks, and 3) DNA without either gap or nick (51). This study reported localized kinks formed in gapped DNA only, indicating that flexible defects were not excited in either nicked or nick-free DNA minicircles. However, as cryo-electron microscopy requires a rapid (milliseconds) freezing step of the DNA samples, one cannot preclude the possibility that an excited defect before cryo freezing could reanneal during freezing process. Therefore, the results from this imaging study cannot be directly compared with results from previous DNA looping experiments using similar length of DNA.

Besides the aforementioned experimental efforts, mechanics of sharply bent DNA was also investigated using full-atom MD simulations. Unstacked kinks were observed to form in 94 bp nick-free DNA minicircles at 300 K using Parm94 force field (52). However, it has been known that *B*-DNA simulated using Parm94 have overpopulated α/γ transitions and geometric deviations from *B*-DNA (31,53); therefore, it is unclear whether the observed defect excitation was caused by use of the Parm94 force field or it was an intrinsic elastic response of DNA.

Is there any evidence supporting nick-independent flexible defect excitation in ~100 bp DNA loops? To our knowledge, there are two pieces of evidence. A recent full-atom MD simulation using Parm99 with ParmBSC0 correction reported that deviation from the canonical WLC model occurred at bending angles $>50^\circ$ with a short DNA fragment of 15 bp (14 basepair steps). This level of bending is comparable to that in a 94 bp DNA loop in a planar circular conformation (i.e., $14/94 \times 360^\circ \approx 54^\circ$); therefore, this suggests that defects could potentially be excited inside DNA under a similar level of bending constraints (54). In addition, a *j*-factor measurement by Forties et al. (42) reported values slightly (less than fivefold) greater than the WLC prediction under the Ω-boundary condition on 116 bp DNA at temperatures above 30°C. The anomalous elasticity was observed for a DNA sequence containing eight TAT repeats, which creates 16 thermally weak AT basepair steps (33), but not for another DNA of the same length lacking such TAT repeats even at 37°C. As the observed anomaly depends on the presence of multiple TAT repeats inside DNA, their results cannot be explained by nick-dependent defect excitation. However, the strong dependence on the presence of multiple TAT repeats raises the question whether the same mechanism could explain the observed mechanical anomaly in other DNA cyclization experiments, as DNAs used in these experiments do not contain such specifically inserted weak basepair repeats (8,9,17,22).

Taken together, our simulations suggest that when a looped short DNA contains nicks, the nicks have the weakest mechanical stability and are prone to develop flexible defects compared to other sites in the DNA. However, as defect excitations at the nicks and in the nick-free DNA region are in thermodynamic competition, which is a predominant factor is not trivial. This obviously depends on the number of weak basepair steps in the nick-free DNA region. A crudest estimate of the possibility P of having at least one disrupted weak basepair steps is: $P = 1 - (1 - p)^N$, where p is the probability of a particular weak basepair step in the disrupted state and N is the number of weak basepair steps. As P increases with N, at large N values defect excitation at such weak basepair steps may be able to outcompete that at the nicks and becomes the dominant factor. Therefore, their competition likely depends on many solution factors (such as temperature, salt, and pH that affect DNA basepair stability), sequence composition, size of DNA (the shorter the less N of weak basepair steps), and the level of bending. In addition, for looped DNA the level of twist has a significant effect on DNA basepair stability (55–57). Considering the importance of this level of DNA bending in ~100 bp loops, the outstanding scientific controversy it has caused and the complex dependence on the above-mentioned experimental

conditions, new experiments using nick-free DNA are warranted to readdress this important question by systematically elucidating the roles of each of these contributing factors.

SUPPORTING MATERIAL

Supporting Materials and Methods, Supporting Discussion, eleven figures and one table are available at http://www.biophysj.org/biophysj/supplemental/S0006-3495(15)01055-3.

AUTHOR CONTRIBUTIONS

J.Y., P.D., J.R.C.v.d.M. conceived the study; P.C. and L.D. performed the MD simulation; P.C., J.Y., and H.C. interpreted and analyzed the data; P.C. and J.Y. wrote the article.

ACKNOWLEDGMENTS

The authors are grateful to John Marko (Northwestern University) and Ralf Bundschuh (Ohio State University) for valuable discussions.

The work is funded by the Mechanobiology Institute at the National University of Singapore, by the Ministry of Education Singapore Academic Research Fund Tier 2 (grant No. MOE2013-T2-1-154) and Tier 3 (grant No. MOE2012-T3-1-001) (to J.Y.), and by the National Research Foundation Singapore through the Singapore-MIT Alliance for Research and Technology's research program in BioSystems and Micromechanics (to P.D.).

SUPPORTING CITATIONS

References (58–65) appear in the Supporting Material.

REFERENCES

1. Richmond, T. J., and C. A. Davey. 2003. The structure of DNA in the nucleosome core. *Nature.* 423:145–150.
2. Oehler, S., M. Amouyal, …, B. Müller-Hill. 1994. Quality and position of the three lac operators of *E. coli* define efficiency of repression. *EMBO J.* 13:3348–3355.
3. Hagerman, P. J. 1988. Flexibility of DNA. *Annu. Rev. Biophys. Biophys. Chem.* 17:265–286.
4. Shore, D., J. Langowski, and R. L. Baldwin. 1981. DNA flexibility studied by covalent closure of short fragments into circles. *Proc. Natl. Acad. Sci. USA.* 78:4833–4837.
5. Doi, M., and S. F. Edwards. 1986. The Theory of Polymer Dynamics. Clarendon Press, Oxford, UK.
6. Smith, S. B., L. Finzi, and C. Bustamante. 1992. Direct mechanical measurements of the elasticity of single DNA molecules by using magnetic beads. *Science.* 258:1122–1126.
7. Marko, J. F., and E. D. Siggia. 1995. Stretching DNA. *Macromolecules.* 28:8759–8770.
8. Cloutier, T. E., and J. Widom. 2004. Spontaneous sharp bending of double-stranded DNA. *Mol. Cell.* 14:355–362.
9. Vafabakhsh, R., and T. Ha. 2012. Extreme bendability of DNA less than 100 base pairs long revealed by single-molecule cyclization. *Science.* 337:1097–1101.
10. Luger, K., A. W. Mäder, …, T. J. Richmond. 1997. Crystal structure of the nucleosome core particle at 2.8 Å resolution. *Nature.* 389:251–260.
11. Davey, C. A., D. F. Sargent, …, T. J. Richmond. 2002. Solvent mediated interactions in the structure of the nucleosome core particle at 1.9 Å resolution. *J. Mol. Biol.* 319:1097–1113.
12. Shore, D., and R. L. Baldwin. 1983. Energetics of DNA twisting. I. Relation between twist and cyclization probability. *J. Mol. Biol.* 170:957–981.
13. Du, Q., C. Smith, …, A. Vologodskii. 2005. Cyclization of short DNA fragments and bending fluctuations of the double helix. *Proc. Natl. Acad. Sci. USA.* 102:5397–5402.
14. Roll, C., C. Ketterlé, …, Y. Boulard. 1998. Conformations of nicked and gapped DNA structures by NMR and molecular dynamic simulations in water. *Biochemistry.* 37:4059–4070.
15. Hyz, K., W. Bocian, …, L. Kozerski. 2011. A dumbbell double nicked duplex dodecamer DNA with a PEG6 tether. *Org. Biomol. Chem.* 9:4481–4486.
16. Taylor, W. H., and P. J. Hagerman. 1990. Application of the method of phage T4 DNA ligase-catalyzed ring-closure to the study of DNA structure. II. NaCl-dependence of DNA flexibility and helical repeat. *J. Mol. Biol.* 212:363–376.
17. Cloutier, T. E., and J. Widom. 2005. DNA twisting flexibility and the formation of sharply looped protein-DNA complexes. *Proc. Natl. Acad. Sci. USA.* 102:3645–3650.
18. Yan, J., and J. F. Marko. 2004. Localized single-stranded bubble mechanism for cyclization of short double helix DNA. *Phys. Rev. Lett.* 93:108108.
19. Yan, J., R. Kawamura, and J. F. Marko. 2005. Statistics of loop formation along double helix DNAs. *Phys. Rev. E Stat. Nonlin. Soft Matter Phys.* 71:061905.
20. Wiggins, P. A., R. Phillips, and P. C. Nelson. 2005. Exact theory of kinkable elastic polymers. *Phys. Rev. E Stat. Nonlin. Soft Matter Phys.* 71:021909.
21. Destainville, N., M. Manghi, and J. Palmeri. 2009. Microscopic mechanism for experimentally observed anomalous elasticity of DNA in two dimensions. *Biophys. J.* 96:4464–4469.
22. Le, T. T., and H. D. Kim. 2014. Probing the elastic limit of DNA bending. *Nucleic Acids Res.* 42:10786–10794.
23. Chen, H., and J. Yan. 2008. Effects of kink and flexible hinge defects on mechanical responses of short double-stranded DNA molecules. *Phys. Rev. E Stat. Nonlin. Soft Matter Phys.* 77:041907.
24. Vologodskii, A., Q. Du, and M. D. Frank-Kamenetskii. 2013. Bending of short DNA helices. *Artif. DNA PNA XNA.* 4:1–3.
25. Lu, X.-J., and W. K. Olson. 2003. 3DNA: a software package for the analysis, rebuilding and visualization of three-dimensional nucleic acid structures. *Nucleic Acids Res.* 31:5108–5121.
26. Jorgensen, W. L., J. Chandrasekhar, …, M. L. Klein. 1983. Comparison of simple potential functions for simulating liquid water. *J. Chem. Phys.* 79:926–935.
27. Hess, B., C. Kutzner, …, E. Lindahl. 2008. GROMACS 4: algorithms for highly efficient, load-balanced, and scalable molecular simulation. *J. Chem. Theory Comput.* 4:435–447.
28. van der Spoel, D., E. Lindahl, …, H. J. C. Berendsen. 2005. GROMACS: fast, flexible, and free. *J. Comput. Chem.* 26:1701–1718.
29. Pronk, S., S. Páll, …, E. Lindahl. 2013. GROMACS 4.5: a high-throughput and highly parallel open source molecular simulation toolkit. *Bioinformatics.* 29:845–854.
30. Cheatham, T. E., 3rd, P. Cieplak, and P. A. Kollman. 1999. A modified version of the Cornell et al. force field with improved sugar pucker phases and helical repeat. *J. Biomol. Struct. Dyn.* 16:845–862.
31. Pérez, A., I. Marchán, …, M. Orozco. 2007. Refinement of the AMBER force field for nucleic acids: improving the description of α/γ conformers. *Biophys. J.* 92:3817–3829.
32. Fonseca Guerra, C., F. M. Bickelhaupt, …, E. J. Baerends. 1999. The nature of the hydrogen bond in DNA base pairs: the role of charge transfer and resonance assistance. *Chemistry.* 5:3581–3594.
33. SantaLucia, J., Jr. 1998. A unified view of polymer, dumbbell, and oligonucleotide DNA nearest-neighbor thermodynamics. *Proc. Natl. Acad. Sci. USA.* 95:1460–1465.

34. Kumar, S., J. M. Rosenberg, …, P. A. Kollman. 1992. The weighted histogram analysis method for free-energy calculations on biomolecules. I. The method. *J. Comput. Chem.* 13:1011–1021.

35. Hub, J. S., B. L. de Groot, and D. van der Spoel. 2010. g_wham—a free weighted histogram analysis implementation including robust error and autocorrelation estimates. *J. Chem. Theory Comput.* 6:3713–3720.

36. Olson, W. K., M. Bansal, …, H. M. Berman. 2001. A standard reference frame for the description of nucleic acid base-pair geometry. *J. Mol. Biol.* 313:229–237.

37. Bustamante, C., J. F. Marko, …, S. Smith. 1994. Entropic elasticity of λ-phage DNA. *Science.* 265:1599–1600.

38. Harrison, R. M., F. Romano, …, J. P. K. Doye. 2015. Coarse-grained modelling of strong DNA bending I: thermodynamics and comparison to an experimental "molecular vice". *arXiv:1506.09005*.

39. Harrison, R. M., F. Romano, …, J. P. K. Doye. 2015. Coarse-grained modelling of strong DNA bending II: cyclization. *arXiv:1506.09008*.

40. Protozanova, E., P. Yakovchuk, and M. D. Frank-Kamenetskii. 2004. Stacked-unstacked equilibrium at the nick site of DNA. *J. Mol. Biol.* 342:775–785.

41. Yakovchuk, P., E. Protozanova, and M. D. Frank-Kamenetskii. 2006. Base-stacking and base-pairing contributions into thermal stability of the DNA double helix. *Nucleic Acids Res.* 34:564–574.

42. Forties, R. A., R. Bundschuh, and M. G. Poirier. 2009. The flexibility of locally melted DNA. *Nucleic Acids Res.* 37:4580–4586.

43. Shimada, J., and H. Yamakawa. 1984. Ring-closure probabilities for twisted wormlike chains. Application to DNA. *Macromolecules.* 17:689–698.

44. Qu, H., C.-Y. Tseng, …, G. Zocchi. 2010. The elastic energy of sharply bent nicked DNA. *Europhys. Lett.* 90:18003.

45. Qu, H., Y. Wang, …, G. Zocchi. 2011. Critical torque for kink formation in double-stranded DNA. *Phys. Rev. X.* 1:021008.

46. Shroff, H., B. M. Reinhard, …, J. Liphardt. 2005. Biocompatible force sensor with optical readout and dimensions of 6 nm^3. *Nano Lett.* 5:1509–1514.

47. Du, Q., A. Kotlyar, and A. Vologodskii. 2008. Kinking the double helix by bending deformation. *Nucleic Acids Res.* 36:1120–1128.

48. Vologodskii, A., and M. D. Frank-Kamenetskii. 2013. Strong bending of the DNA double helix. *Nucleic Acids Res.* 41:6785–6792.

49. Wiggins, P. A., T. van der Heijden, …, P. C. Nelson. 2006. High flexibility of DNA on short length scales probed by atomic force microscopy. *Nat. Nanotechnol.* 1:137–141.

50. Mazur, A. K., and M. Maaloum. 2014. DNA flexibility on short length scales probed by atomic force microscopy. *Phys. Rev. Lett.* 112:068104.

51. Demurtas, D., A. Amzallag, …, A. Stasiak. 2009. Bending modes of DNA directly addressed by cryo-electron microscopy of DNA minicircles. *Nucleic Acids Res.* 37:2882–2893.

52. Lankaš, F., R. Lavery, and J. H. Maddocks. 2006. Kinking occurs during molecular dynamics simulations of small DNA minicircles. *Structure.* 14:1527–1534.

53. Pérez, A., F. Lankaš, …, M. Orozco. 2008. Towards a molecular dynamics consensus view of *B*-DNA flexibility. *Nucleic Acids Res.* 36:2379–2394.

54. Curuksu, J., M. Zacharias, …, K. Zakrzewska. 2009. Local and global effects of strong DNA bending induced during molecular dynamics simulations. *Nucleic Acids Res.* 37:3766–3773.

55. Harris, S. A., C. A. Laughton, and T. B. Liverpool. 2008. Mapping the phase diagram of the writhe of DNA nanocircles using atomistic molecular dynamics simulations. *Nucleic Acids Res.* 36:21–29.

56. Liverpool, T. B., S. A. Harris, and C. A. Laughton. 2008. Supercoiling and denaturation of DNA loops. *Phys. Rev. Lett.* 100:238103.

57. Mitchell, J. S., and S. A. Harris. 2013. Thermodynamics of writhe in DNA minicircles from molecular dynamics simulations. *Phys. Rev. Lett.* 110:148105.

58. Yamakawa, H. 1972. Statistical mechanics of wormlike chains. II. Excluded volume effects. *J. Chem. Phys.* 57:2843–2854.

59. Lu, X.-J., and W. K. Olson. 2008. 3DNA: a versatile, integrated software system for the analysis, rebuilding and visualization of three-dimensional nucleic-acid structures. *Nat. Protoc.* 3:1213–1227.

60. Bussi, G., D. Donadio, and M. Parrinello. 2007. Canonical sampling through velocity rescaling. *J. Chem. Phys.* 126:014101.

61. Parrinello, M. 1981. Polymorphic transitions in single crystals: a new molecular dynamics method. *J. Appl. Phys.* 52:7182–7190.

62. Clowney, L., S. C. Jain, …, H. M. Berman. 1996. Geometric parameters in nucleic acids: nitrogenous bases. *J. Am. Chem. Soc.* 118:509–518.

63. Horn, B. K. P. 1987. Closed-form solution of absolute orientation using unit quaternions. *J. Opt. Soc. Am. A.* 4:629–642.

64. Torrie, G. M., and J. P. Valleau. 1977. Nonphysical sampling distributions in Monte Carlo free-energy estimation: umbrella sampling. *J. Comput. Phys.* 23:187–199.

65. Cocco, S., J. Yan, …, J. F. Marko. 2004. Overstretching and force-driven strand separation of double-helix DNA. *Phys. Rev. E Stat. Nonlin. Soft Matter Phys.* 70:011910.

Supporting Material for: Revisiting the Anomalous Bending Elasticity of Sharply Bent DNA

Peiwen Cong,[1,2,3] Liang Dai,[4] Hu Chen,[5] Johan R. C. van der Maarel,[3] Patrick S. Doyle,[4,6] Jie Yan,[1,3,4,7,⋆]

[1]Mechanobiology Institute, [2]Singapore-MIT Alliance, and [3]Department of Physics, National University of Singapore, Singapore; [4]BioSystems and Micromechanics IRG, Singapore-MIT Alliance for Research and Technology Centre, Singapore; [5]Department of Physics, Xiamen University, Xiamen, Fujian, China; [6]Department of Chemical Engineering, Massachusetts Institute of Technology, Cambridge, Massachusetts; [7]Centre for BioImaging Sciences, National University of Singapore, Singapore

Supporting Figures

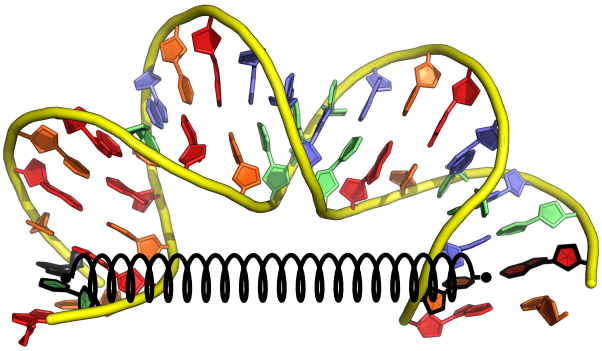

FIGURE S1 Initial smoothly bent DNA conformation generated by `X3DNA`. This initial conformation has an overall bending angle of $\sim 160°$. A constraining spring is connected to the bases of second and second-last basepairs (highlighted with black outlines) to actively pull the DNA ends inward. Note that the nucleotides are colored by sequence, `A` in blue, `T` in green, `G` in red and `C` in orange, while sugar-phosphate backbones are colored yellow.

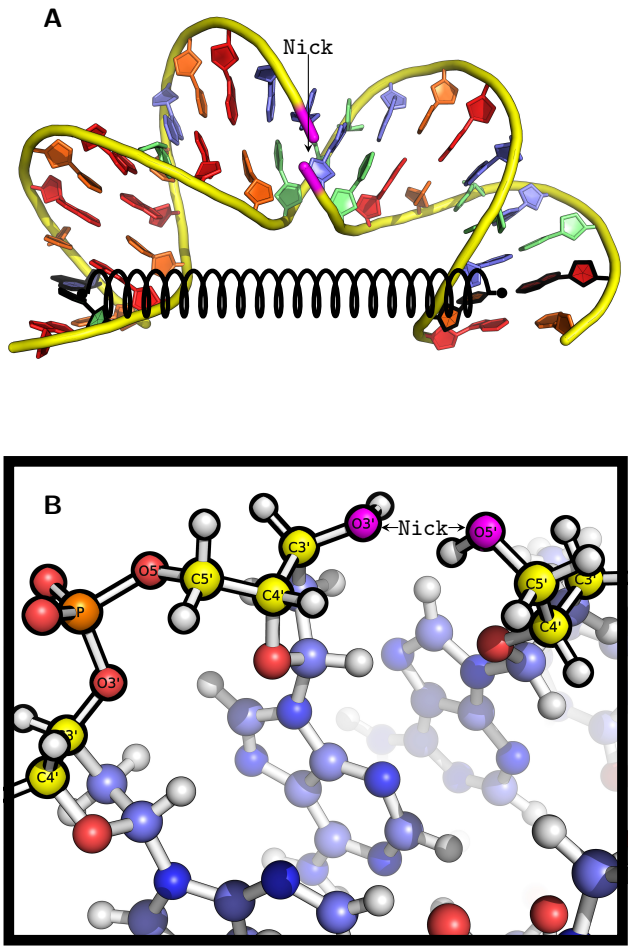

FIGURE S2 Nicked DNA construct with nick after the 11^{th} basepair. (*A*) The initial smoothly bent DNA containing a nick between the 11^{th} and 12^{th} basepairs in Strand I, highlighted in magenta. (*B*) Magnification of the nicked site, where the phosphodiester bonds were cleaved and the entire phosphate group was removed, leaving the O3' and O5' atoms (magenta) hydrolyzed. The backbone carbon atoms are colored yellow, phosphate atoms are colored orange and oxygen atoms are colored red. The parameters describing resulting terminal nucleotide residues (-OH) at the nick are included in Parm99 force field with ParmBSC0 corrections.

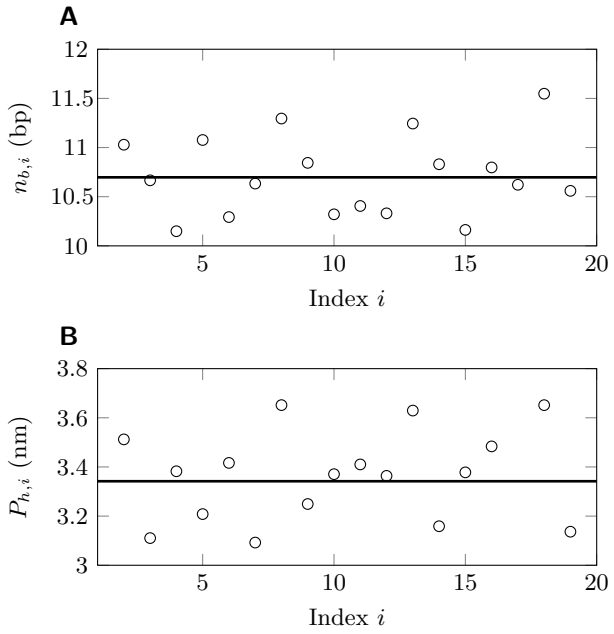

FIGURE S3 Helical parameters for *B*-DNA without constraints. (*A*) Helical repeat, $n_{b,i}$ and (*B*) helical pitch, $P_{h,i}$ along DNA were calculated using average twist and rise at particular site i over the last 20 ns out of 70 ns unconstrained simulation. Black lines show the global mean values of 10.70 ± 1.53 bp and 3.34 ± 0.67 nm respectively, obtained through $n_b = 2\pi / \langle \Omega \rangle$ and $P_h = 2\pi \langle D_z \rangle / \langle \Omega \rangle$, where Ω is twist angle, D_z is rise per basepair step. Note that the values after $\pm$ sign are the corresponding standard deviations of uncorrelated structure representatives. $n_{b,i}$ and $P_{h,i}$ are all around their global mean values, which indicates the homogeneity of unconstrained DNA.

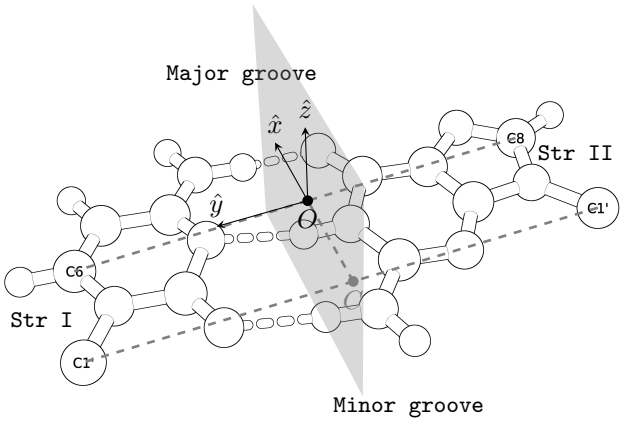

FIGURE S4 Basepair reference frame. Reference frame for ideal Watson-Crick basepair using C≡G basepair as an example, and only complementary bases are shown. The coordinate is defined by four atoms, C1', C6 from pyrimidine nucleotides (C and T), and C1', C8 from purine nucleotides (G and A). The grey plane, which is the perpendicular bisector of the line segment $\overline{\text{(C1' C1')}}$ at the midpoint C, intersects with the line segment $\overline{\text{(C6 C8)}}$ at O. x-axis directs from C to O. y-axis is parallel to $\overline{\text{(C1' C1')}}$, pointing towards the Strand I. z-axis is $\hat{z} = \hat{x} \times \hat{y}$.

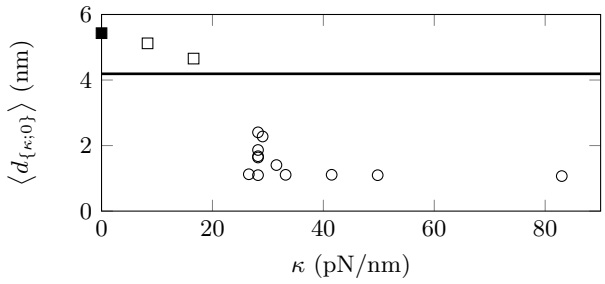

FIGURE S5 Mean values of end-to-end distances $\langle d_{\{\kappa;0\}} \rangle$ under various spring constrains. They were averaged over last 20 ns for each simulation. $\langle d \rangle$ with $\kappa = 0$ pN/nm from the unconstrained simulation (■) is shown as control. $\langle d_{\{\kappa;0\}} \rangle$ with $\kappa < 20.0$ pN/nm (□) are longer than d_{ini} (black line), shorted than control, and negatively correlated with κ. $\langle d_{\{\kappa;0\}} \rangle$ with $\kappa > 25.0$ pN/nm (○) are much shorter than d_{ini} and uncorrelated with κ.

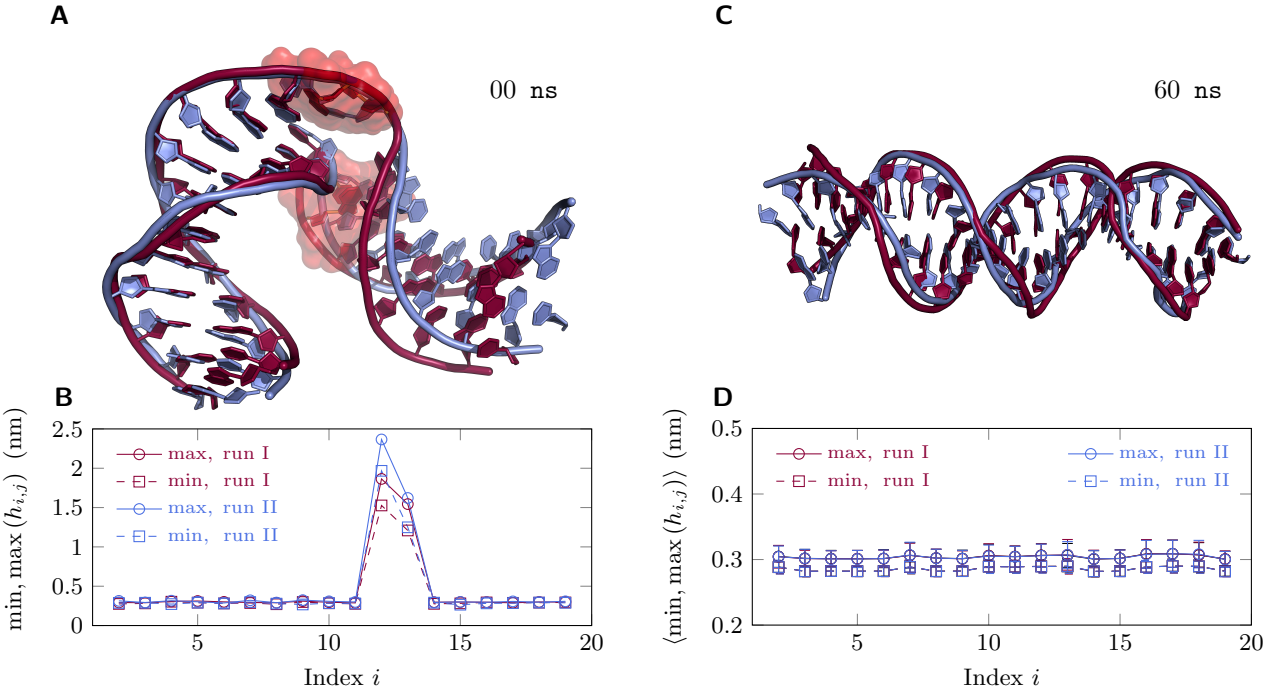

FIGURE S6 Reversibility of DNA defects. Two 70 ns simulations were conducted to check the reversibility of defects once the sharp bending constraint was removed. Runs I (dark red) and II (light blue) were started from two different defect-containing DNAs induced by sharp bending. (A) The initial atomic structures of runs I and II both with defected 12^{th} and 13^{th} basepairs highlighted with the red surfaces. (B) Their corresponding hydrogen bonding distances, $\min, \max(h_{i,j})$ plotted against i ($i = 2, 3, \cdots, 19$) at 0 ns. (C) The snapshots taken at 60 ns after the simulations began, which show straightened B-form conformations. (D) The resulting hydrogen bonding profiles, $\langle \min, \max(h_{i,j}) \rangle$ along DNA averaged in $50 - 70$ ns trajectories overlap with that of control, which was obtained from previous non-constrained simulation for intact B-form DNA (black). Thus, the sharp bending induced defects are transient, and are able to restore into B-form given that the bending constraint is removed.

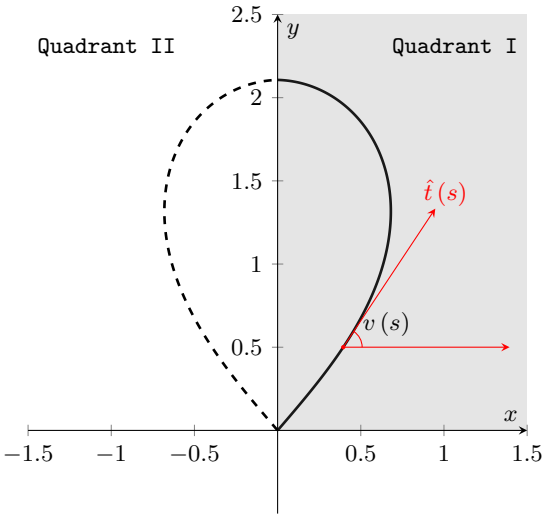

FIGURE S7 Energy minimal rigid path of short DNA fragment. Without considering thermal fluctuations, a planar looped rigid homogeneous polymer under free boundary conditions forms a symmetric path, whose energy minimal conformation assumes a teardrop shape. By defining the angle between unit tangent vector $\hat{t}(s)$ (along the half path in Quadrant I) and x-axis as $\upsilon(s)$, it relates to curvature as, $L^2\left(\partial\hat{t}(s)/\partial s\right)^2 = -\lambda\cos\left(\upsilon(s)\right) + c$, where L is the contour length, $\lambda > 0$ is Lagrange multiplier, and $c > 0$ is integration constant (1). And this implies maximized curvature at its center, as $\upsilon\left(L/2\right) = \pi$ by symmetry. Here, the contour length was set to be $L = d_e = 5.43$ nm same as our simulated equilibrium length of 20 bp DNA, whose two termini make an angle of $\theta = 81°24'$ in this teardrop shape.

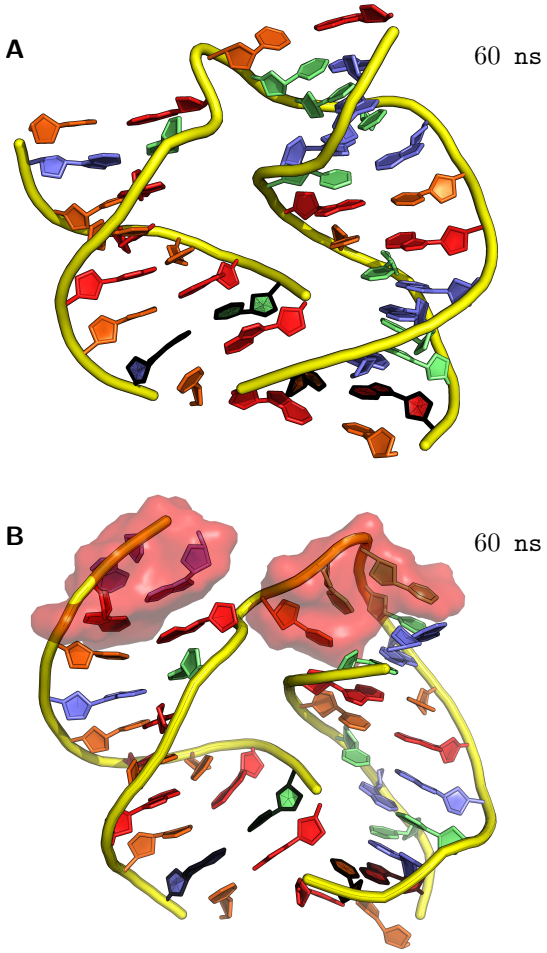

FIGURE S8 Atomic structures for unstacked and peeled nick-containing DNAs. (*A*) A snapshot at $t = 60$ ns demonstrates an unstacked case, which was extracted from the $\{28.2; 0\}$-constrained simulation of nicked DNA with nick on Strand I between the 8^{th} and 9^{th} basepairs. (*B*) A snapshot at $t = 60$ ns shows a peeled case, which was clipped from the $\{28.2; 0\}$-constrained trajectory of nicked DNA with nick on Strand I between the 11^{th} and 12^{th} basepairs. The red surfaces indicate the peeled Strand I from the nick and their unpaired complementary bases at the disrupted 9^{th}, 10^{th} and 11^{th} basepairs.

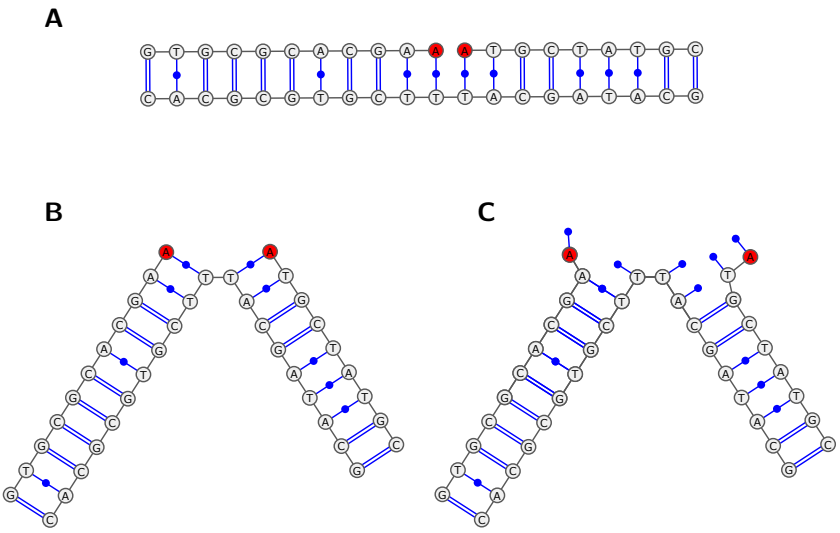

FIGURE S9 Illustrations for nicked DNA with different categories of non-covalent topologies. (*A*) Type A shows the intact nicked DNA with both intact hydrogen bonding and basepair stacking. (*B*) Type B represents the unstacked nicked DNA with disrupted basepair stacking only at nicked position. (*C*) Type C indicates a particular case of the peeled nicked DNA with both nicked ends split, resulting in both disrupted base-stacking and base-pairing around the nicked site. These illustrations use non-helical representations of nicked DNA with nicks after the 11^{th} basepair as examples.

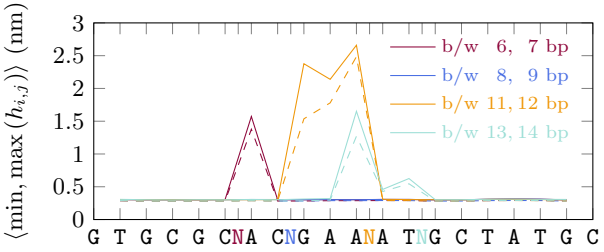

FIGURE S10 Hydrogen bonding profiles for the four nicked DNAs under $\{28.2; 0\}$**.** The hydrogen bonding profiles, $\langle \min, \max (h_{i,j}) \rangle$ plotted against basepair index i averaged over the last 20 ns of 70 ns trajectories for four independent simulations with nick right after the 6^{th}, 8^{th}, 11^{th} and 13^{th} basepairs. Although their C4' inter-base distance profiles in main text have already indicated the presences of base-stacking disruptions at the nicked sites, these hydrogen bonding profiles further reveal the existence of two distinctive types of disruptions: clean unstacking at nicked site (i.e., with totally intact hydrogen bonding) in the case of nick after the 8^{th} basepair; and unstacking accompanied with peeling from nicked sites (i.e., with locally disrupted hydrogen bonding) in the case of nicks after the 6^{th}, 11^{th} and 13^{th} basepairs.

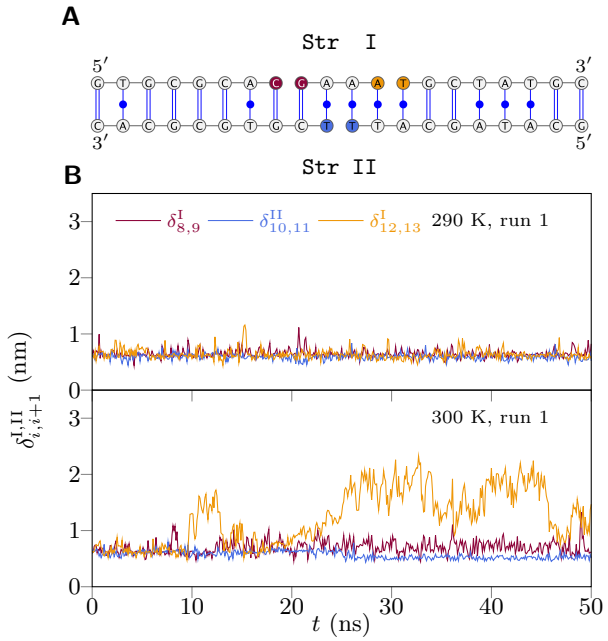

FIGURE S11 Temprature effects on nick unstacking. At each temperature of 290, 300 and 310 K, four independent 50 ns trajectories under the spring constraint of $\{248.9; 4.20\}$ were generated for triple-nicked DNA. (A) An illustration of DNA with three nicks located between the 8^{th} and 9^{th} basepairs on Strand I, the 10^{th} and 11^{th} basepairs on Strand II, the 12^{th} and 13^{th} basepairs on Strand I. The basepair index, i, is counted from $5'$ end of Strand I as 1 to 20. (B) The dynamics of inter-base distances, $\delta^{\mathrm{I}}_{8,9}$, $\delta^{\mathrm{II}}_{10,11}$ and $\delta^{\mathrm{I}}_{12,13}$, that straddling the nicks show clear differences between 290 and 300 K, where lower temperature inhibits unstacking. Note that only two out of twelve simulation dynamics are plotted here as examples.

Supporting Table

	Case *i*		Case *ii*		Case *iii*	
Bp step	Tilt	Roll	Tilt	Roll	Tilt	Roll
01 GT/AC	0.51	-3.81	-3.62	1.23	2.73	2.68
02 TG/CA	-1.73	-3.42	-2.27	3.09	3.77	0.66
03 GC/GC	-3.35	-1.83	-0.15	3.84	3.49	-1.59
04 CG/CG	-3.82	0.38	2.05	3.23	1.96	-3.28
05 GC/GC	-2.92	2.47	3.52	1.50	-0.23	-3.82
06 CA/TG	-1.01	3.70	3.75	-0.75	-2.34	-3.03
07 AC/GT	1.26	3.62	2.68	-2.75	-3.65	-1.16
08 CG/CG	3.08	2.27	0.65	-3.78	-3.66	1.12
09 GA/TC	3.83	0.12	-1.59	-3.48	-2.40	2.98
10 AA/TT	3.23	-2.06	-3.29	-1.96	-0.27	3.83
11 AA/TT	1.50	-3.53	-3.83	0.23	1.92	3.31
12 AT/AT	-0.76	-3.76	-3.00	2.37	3.46	1.64
13 TG/CA	-2.76	-2.66	-1.15	3.65	3.79	-0.61
14 GC/GC	-3.77	-0.64	1.13	3.66	2.77	-2.64
15 CT/AG	-3.48	1.62	3.00	2.38	0.79	-3.75
16 TA/TA	-1.95	3.29	3.82	0.27	-1.47	-3.53
17 AT/AT	0.26	3.82	3.30	-1.94	-3.21	-2.08
18 TG/CA	2.38	3.02	1.63	-3.46	-3.83	0.10
19 GC/GC	3.64	1.13	-0.63	-3.77	-3.10	2.25

TABLE S1 Tilt and roll parameters for constructing directionally bent initial conformations. The rotational parameters, tilt and roll, describe the relative rotational angles between consecutive basepair reference frames, along x-axis and y-axis respectively. The constant $\sqrt{\text{tilt}^2 + \text{roll}^2}$ maintains a uniform bending, while their systematic alternations alone helix produce a constant bending direction. These three sets of tilt and roll angles (i.e., in units of degree) generate DNA initial conformations bending towards distinctive directions as shown in main text Fig. 9, whose end-to-end vectors projected onto common 1$^{\text{st}}$ basepair plane are evenly separated by 120°.

Supporting Methods: Simulation and analysis details

Unit cell preparation

Before starting any simulation, a basic simulating unit (i.e., unit cell) was properly constructed. Firstly, an initial atomic DNA structure with targeted sequence and shape was generated using `X3DNA` (2). Secondly, this initial structure was centered within a minimal unit cell. Our unit cell usually takes rhombic dodecahedron shape (i.e., $\sim 71\%$ of cubic unit cell volume), whose inscribed sphere diameter equals the largest DNA extension plus an additional 3.2 nm for buffering. Next, this unit cell was further prepared by filling the empty space with TIP3P water (3), neutralizing the negative charges on DNA using sodium counter-ions, and replacing some water molecules with sodium chloride to achieve 150 mM ionic strength. Lastly, it was finalized by energy minimization using the steepest descent method to remove any energy unfavorable close contacts.

Based on this prepared unit cell, molecular trajectories were self-evolved according to Newton's law of motion, given a set of initial velocities (randomly sampled from Maxwell-Boltzmann distribution) and external constraints, such as contractile springs for inducing bending. Before collecting conformational evolutions, the unit cell was brought to correct ensemble using 200 ps velocity rescaling and 200 ps Parrinello-Rahman pressure coupling simulations (4, 5).

Basepair coordinates

Assigning a basepair coordinate to the group of thermally fluctuated atoms is the key to bridge from MD raw trajectories to DNA macroscopic behaviors, such as bending dynamics.

An ideal Watson-Crick basepair (6) was fitted to each observed instantaneous atomic arrangements during MD simulations by minimizing the sum of squares of their residual errors. This least-square fitting was implemented by Horn in 1987 (7) through finding a closed-form solution of the ideal basepair absolute orientation against such instantaneous atomic arrangements. A sketch of this ideal basepair coordinates is shown (Fig. S4). For this `G≡C` Watson-Crick basepair, a right-handed coordinate frame as described by Olson et al. (8) was attached to it, with $\hat{x}_i$ pointing to the major groove, $\hat{y}_i$ pointing to the backbone of the top strand, and $\hat{z}_i = \hat{x}_i \times \hat{y}_i$ describing the normal direction of the Watson-Crick basepair, where i denotes the i^{th} basepair. This process was achieved using `X3DNA` software during our analysis (2, 9).

After this, some macroscopic configuration information was extrapolated using local coordinates. For example, the bending angle between i^{th} and $(i+\Delta)^{\text{th}}$ basepairs, defined by $\theta_{i,i+\Delta} = \cos^{-1}\left(\hat{z}_i \bullet \hat{z}_{i+\Delta}\right)$, where $i = 2, 3, \cdots, 19-\Delta$, were calculated for any instantaneous conformation of DNA in some simulations.

Umbrella sampling

During umbrella sampling, a series of springs indexed by m, each with a finite equilibrium length of l_m and fixed spring constant $\kappa = 248.9$ pN/nm, were used to induce DNA bending (i.e., $\{248.9; l_m\}$). For each $\{248.9; l_m\}$-constrained simulation, the biased distribution of the distance fluctuation, $\rho_{\{\kappa;l_m\}}(d)$, was obtained. Theoretically, the regional unbiased $\mathcal{A}(d)$ can be obtained by $\mathcal{A}(d) = -\beta^{-1} \ln \rho_{\{\kappa;l_m\}}(d) - (\kappa/2)(d-l_m)^2 + \mathcal{A}_{\{\kappa;l_m\}}$, where $\mathcal{A}_{\{\kappa;l_m\}}$ is an undetermined shift. Here, the unbiased distribution of the distance fluctuation $\rho(d)$ and global $\mathcal{A}(d)$ (i.e., reference to its global energy minimal state) were obtained by weighted histogram analysis method using `g_wham` (10, 11), which optimizes the shifts to minimize the statistical errors of $\sigma^2(\rho(d))$ (12). During our analysis, $\mathcal{A}(d)$ was evaluated at 200 discrete points for the each type of DNA, then further smoothed by cubic spline interpolation, from which the continuous force-distance curve could be obtained by $f(d) = -\partial\mathcal{A}(d)/\partial d$.

Supporting Discussion: Active bending experiment by Shroff et al.

In the experiment by Shroff et al., a nick-free 25 bp dsDNA fragment was bent by a 12 nt ssDNA connected at the two dsDNA ends (13). Assuming dsDNA is intact, its internal tension is expected to be around the bucking transition force of ~ 30 pN. This corresponds to ssDNA separation of ~ 6 nm based on phenomenological ssDNA force extension model (14), similar to that between two points separated by 24 basepair steps in a 64 bp DNA minicircle with a planar circle conformation (i.e., $L \sin(24\pi/64)/\pi \approx 6$ nm, where L is the contour length of the 64 bp minicircle). However, the measured tension in the ssDNA was shown to be 6 ± 5 pN, a few times smaller than the aforementioned critical buckling force. Thus, the distance between the two dsDNA ends was estimated to be only < 4 nm, which revealed DNA anomalous elastic responses.

Supporting References

[1] Yamakawa, H., 1972. Statistical mechanics of wormlike chains. II. Excluded volume effects. *J. Chem. Phys.* 57:2843–2854.

[2] Lu, X.-J., and W. K. Olson, 2008. 3DNA: a versatile, integrated software system for the analysis, rebuilding and visualization of three-dimensional nucleic-acid structures. *Nat. Protoc.* 3:1213–1227.

[3] Jorgensen, W. L., J. Chandrasekhar, J. D. Madura, R. W. Impey, and M. L. Klein, 1983. Comparison of simple potential functions for simulating liquid water. *J. Chem. Phys.* 79:926–935.

[4] Bussi, G., D. Donadio, and M. Parrinello, 2007. Canonical sampling through velocity rescaling. *J. Chem. Phys.* 126:014101.

[5] Parrinello, M., 1981. Polymorphic transitions in single crystals: A new molecular dynamics method. *J. Appl. Phys.* 52:7182–7190.

[6] Clowney, L., S. C. Jain, A. R. Srinivasan, J. Westbrook, W. K. Olson, and H. M. Berman, 1996. Geometric parameters in nucleic acids: nitrogenous bases. *J. Am. Chem. Soc.* 118:509–518.

[7] Horn, B. K. P., 1987. Closed-form solution of absolute orientation using unit quaternions. *J. Opt. Soc. Am. A.* 4:629–642.

[8] Olson, W. K., M. Bansal, S. K. Burley, R. E. Dickerson, M. Gerstein, S. C. Harvey, U. Heinemann, X.-J. Lu, S. Neidle, Z. Shakked, H. Sklenar, M. Suzuki, C.-S. Tung, E. Westhof, C. Wolberger, and H. M. Berman, 2001. A standard reference frame for the description of nucleic acid base-pair geometry. *J. Mol. Biol.* 313:229–237.

[9] Lu, X.-J., and W. K. Olson, 2003. 3DNA: a software package for the analysis, rebuilding and visualization of three-dimensional nucleic acid structures. *Nucleic Acids Res.* 31:5108–5121.

[10] Kumar, S., J. M. Rosenberg, D. Bouzida, R. H. Swendsen, and P. A. Kollman, 1992. The weighted histogram analysis method for free-energy calculations on biomolecules. I. The method. *J. Comput. Chem.* 13:1011–1021.

[11] Hub, J. S., B. L. de Groot, and D. van der Spoel, 2010. g_wham—a free weighted histogram analysis implementation including robust error and autocorrelation estimates. *J. Chem. Theory Comput.* 6:3713–3720.

[12] Torrie, G. M., and J. P. Valleau, 1977. Nonphysical sampling distributions in Monte Carlo free-energy estimation: Umbrella sampling. *J. Comput. Phys.* 23:187–199.

[13] Shroff, H., B. M. Reinhard, M. Siu, H. Agarwal, A. Spakowitz, and J. Liphardt, 2005. Biocompatible force sensor with optical readout and dimensions of 6 nm^3. *Nano Lett.* 5:1509–1514.

[14] Cocco, S., J. Yan, J.-F. Léger, D. Chatenay, and J. Marko, 2004. Overstretching and force-driven strand separation of double-helix DNA. *Phys. Rev. E Stat. Nonlin. Soft Matter Phys.* 70:011910.